Rattling-enhanced superconductivity in MV$_2$Al$_{20}$ (M = Sc, Lu, Y) intermetallic cage compounds

M. J. Winiarski,[1,*] B. Wiendlocha,[2] M. Sternik,[3] P. Wiśniewski,[4] J. R. O'Brien,[5] D. Kaczorowski,[4] and T. Klimczuk[1,*]

[1]*Faculty of Applied Physics and Mathematics, Gdansk University of Technology, Narutowicza 11/12, 80-233 Gdansk, Poland*

[2]*AGH University of Science and Technology, Faculty of Physics and Applied Computer Science, Aleja Mickiewicza 30, 30-059 Krakow, Poland*

[3]*Institute of Nuclear Physics, Polish Academy of Sciences, Radzikowskiego 152, 31-342 Krakow, Poland*

[4]*Institute for Low Temperature and Structure Research, Polish Academy of Sciences, PNr 1410, 50-950 Wrocław, Poland*

[5]*Off Grid Research, 6501 Goodwin Street, San Diego, California 92111, USA*

Polycrystalline samples of four intermetallic compounds: MV$_2$Al$_{20}$ (M = Sc, Y, La, and Lu) were synthesized using an arc-melting technique. The crystal structures were analyzed by means of powder x-ray diffraction and Rietveld analysis, and the physical properties were studied by means of heat capacity, electrical resistivity, and magnetic susceptibility measurements down to 0.4 K. For ScV$_2$Al$_{20}$, LuV$_2$Al$_{20}$, and YV$_2$Al$_{20}$, superconductivity was observed with critical temperatures T_c = 1.00, 0.57, and 0.60 K, respectively. Superconductivity for the Lu compound is reported. Theoretical calculations of the electronic and phonon structures were conducted in order to analyze the superconductivity and dynamics in ScV$_2$Al$_{20}$, YV$_2$Al$_{20}$, and LuV$_2$Al$_{20}$ and to explain the lack of a superconducting transition in LaV$_2$Al$_{20}$ down to 0.4 K. The results of the experimental and theoretical studies show that all the compounds are weakly coupled type-II BCS superconductors, and reveal the importance of the M-atom anharmonic "rattling" modes for the superconductivity in these materials, which seem to enhance T_c, especially for ScV$_2$Al$_{20}$.

I. INTRODUCTION

The interesting physical behavior that is often observed in cage-type structures frequently originates from the so-called "rattling" effect. In this study we associate rattling with a localized, anharmonic, low frequency, and high amplitude vibration mode, at specific crystallographic site(s), such as at the center of an oversized atomic cage. It is believed that the rattling effect is responsible for superconductivity in β-pyrochlore oxides AOs$_2$O$_6$ (A = K, Rb, Cs) [1,2], the enhancement of the thermoelectric figure of merit in skutterudite and clathrate-based semiconducting thermoelectrics [3,4], and the enhancement of the Sommerfeld coefficient (effective mass) in SmOs$_4$Sb$_{12}$ [5] and PrOs$_4$Sb$_{12}$ [6].

One of the most extensively studied systems is the β-pyrochlore AOs$_2$O$_6$. This family has attracted much attention due to its relatively high superconducting transition temperatures (T_c = 9.6 K for A = K, T_c = 6.4 K for A = Rb, and T_c = 3.25 K for A = Cs [7]), which are clearly linked to the different ionic radii of the rattling ions: the highest T_c is observed for the compound with the smallest alkali cation (KOs$_2$O$_6$), for which the largest vibrational anharmonicity was found in calculations [8]. On the other hand, inelastic neutron scattering measurements done by Mutka *et al.* shown that the dynamics of a group I cation in AOs$_2$O$_6$ is more complicated than a simple single-particle rattling [9]. The electron-phonon coupling in KOs$_2$O$_6$ was found to be exceptionally strong ($\lambda_{el-ph} \approx 2.4$) [10]. All these findings stimulated many theoretical investigations (see, e.g., Refs. [11–15]). A summary and review of experimental and theoretical studies on rattling and its effect on superconductivity in β-pyrochlores can be found in Ref. [16].

A series of studies of superconducting hexa- and dodecaborides showed similar behavior to that of AOs$_2$O$_6$. The boron network in the dodecaboride ZrB$_{12}$ is an inert background for superconductivity, as concluded from the results of the superconducting isotope effect studies on B [17] and Zr [18]. The more than one order of magnitude higher T_c observed for ZrB$_{12}$ (T_c = 6 K) than for LuB$_{12}$ (T_c = 0.44 K) was explained by weaker coupling of the Einstein phonon related to the vibration of the Lu ion to the conduction electrons [19]. Studies on clathrate superconductors Ba$_8$Si$_{46}$ and Ba$_{24}$Si$_{100}$ held by Lortz *et al.* [20] had shown that the main phonon contribution to the electron-phonon coupling arises from low-energy vibrational modes of Ba ions encaged by Si atoms.

The group of isostructural intermetallic ternaries RCr$_2$Al$_{20}$ (R = La-Nd, Gd, Ho, Er) and RV$_2$Al$_{20}$ (R = La-Nd, Gd) was first reported in the late 1960s. In the prototypic CeCr$_2$Al$_{20}$ compound, space group *Fd-3m*, chromium (Wyckoff position 16*d*) and aluminum (16*c*, 48*f*, and 96*g*) atoms form cages with large icosahedral voids occupied by cerium (8*a*). A unit cell of the CeCr$_2$Al$_{20}$-type structure is shown in the inset of Fig. 1. The atomic positions were found to be the same as in the Mg$_3$Cr$_2$Al$_{18}$ [21] and ZrZn$_{22}$ [22,23] intermetallics described earlier. In further studies, CeCr$_2$Al$_{20}$-type (1-2-20) aluminides were synthesized with transition metals of groups 5 and 6 as well with titanium and manganese [24–32]. Depending on the transition metal, different electropositive elements (rare-earth elements, actinides, and Ca) could be introduced to the 8*a* position, with compounds containing 4*d* and 5*d* metals generally forming only with the early lanthanides (La-Sm), Ca, and U [27]. Systematic studies in the 1-2-20 group has led also to the synthesis of RT$_2$Zn$_{20}$ (R = lanthanides, Zr, Hf, Nb and U, T = transition metals of groups 7–10) [33–37] and RT$_2$Cd$_{20}$ (R = rare earth, T = Ni, Pd) [38] intermetallics.

Several superconductors were found among the 1-2-20 intermetallics, i.e., Al$_x$V$_2$Al$_{20}$ [42,43], Ga$_x$V$_2$Al$_{20}$, YV$_2$Al$_{20}$ [44], ScV$_2$Al$_{20}$, and PrTi$_2$Al$_{20}$ [45] within the aluminide group

---

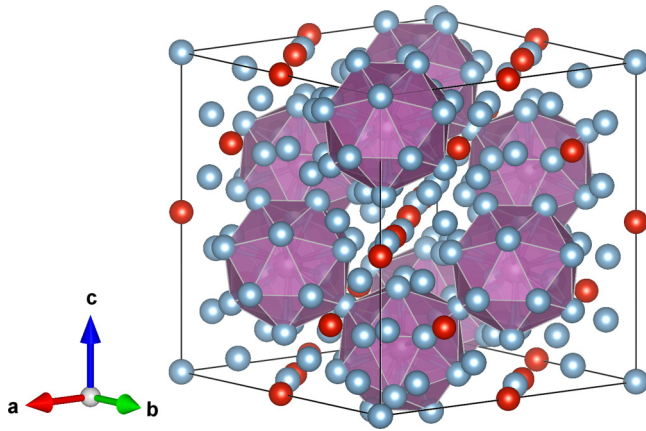*Corresponding authors: mwiniarski@mif.pg.gda.pl; tomasz.klimczuk@pg.gda.pl

FIG. 1. Unit cell of $CeCr_2Al_{20}$-type intermetallics. In the prototypic compound, Ce atoms (violet) occupy Wyckoff position $8a$ $(1/8,1/8,1/8)$ surrounded by Al atoms (blue) in positions $96g$ and $16c$. Cr atoms (red, position $16d$) form a pyrochlore lattice [39]. More views of the $CeCr_2Al_{20}$-type structure are depicted in the Supplemental Material [40]. Image was rendered using VESTA software [41].

and $LaRu_2Zn_{20}$, $LaIr_2Zn_{20}$, $PrIr_2Zn_{20}$ [46], and $PrRh_2Zn_{20}$ [47] amid the Zn-based compounds. In LaV_2Al_{20} a strong diamagnetism was found lately but no superconducting transition was observed down to 0.4 K [48]. The strong Landau-Peierls diamagnetic susceptibility results from the peculiarities of the Fermi surface [49].

In $Al_xV_2Al_{20}$ and $Ga_xV_2Al_{20}$ the link between anharmonic rattling of Al/Ga atoms at $8a$ site and superconductivity was found [16,42–44]. Recently, Koza *et al.* [50,51] investigated the vibrational characteristics of several MV_2Al_{20} (M = Sc, La, Ce, Al, Ga, and Y) by means of inelastic neutron scattering experiments and *ab initio* calculations, showing the anharmonic character of M ($8a$) site potential in case of small cage-filling atoms (M = Al, Ga, Sc) and the importance of $8a$ low-energy phonon modes. On the other hand, Hasegawa *et al.* [52] and Wakiya *et al.* [53] has found by means of computational and experimental methods, respectively, that in $LaRu_2Zn_{20}$ and $LaIr_2Zn_{20}$ the Zn($16c$) low-energy modes dominate the phonon structures.

In this study, a series of MV_2Al_{20} (M = Sc, Y, Lu, La) cage compounds was synthesized and their physical properties were investigated by means of electrical resistivity, magnetic susceptibility, and heat capacity measurements. Superconductivity was observed for ScV_2Al_{20}, YV_2Al_{20}, and LuV_2Al_{20} and was not found for LaV_2Al_{20} down to 0.4 K. Structural studies were performed with powder x-ray diffraction and the data were refined using the Rietveld method [54]. Finally, electronic and phonon structure calculations were carried out and the anharmonicity and electron-phonon coupling coefficients were studied in detail. The theoretical work provides a firm foundation for the interpretation of the experimental observations in terms of the differences between different rattling atoms in the cages.

II. EXPERIMENTAL PROCEDURE

Samples of MV_2Al_{20} were synthesized using a sequential arc-melting technique. Stoichiometric amounts of rare-earth metals (99.9% purity) and vanadium (99.8%) with approximately one third of the total aluminum (99.999%) amount were melted together in an electric arc under a high purity argon atmosphere. In the second step, the remaining aluminum was added. The stepwise process was designed to ensure good homogeneity of samples with high Al content ($\sim$87 at. %). The samples were then remelted three times to homogenize the composition. After each melting, the buttons were weighed to estimate the mass loss and small portions of Al (below 1% of the total aluminum content) were added if needed.

The as-cast samples were sealed in evacuated quartz tubes. Tantalum foil was used as a getter and to prevent a direct contact between the sample and ampoule walls. Sealed ampoules were put in a furnace for three weeks at 650 °C, just below the melting point of Al (661 °C). After annealing, the samples were quenched in water at room temperature.

Powder XRD measurements on powdered annealed samples were conducted on a Bruker D8 diffractometer with monochromatized $CuK_{\alpha1}$ radiation. The results were processed by means of Rietveld refinement using FULLPROF 5.30 software [55]. The initial structural models were derived from the $VAl_{10.1}$ compound structure [42].

Electrical resistivity measurements were conducted on polished samples with Pt contacts glued to the surface using a silver paste. Measurements were done in a Quantum Design Physical Property Measurement System with ^{3}He cooling. Heat capacity measurements were done on small (few milligram) polished samples in the same system using the standard relaxation method as well as dual slope technique [56]. Magnetic susceptibility measurements were carried out in a Quantum Design MPMS-XL SQUID magnetometer equipped with an iQuantum ^{3}He refrigerator.

III. RESULTS

A. Crystal structure

The room temperature powder x-ray diffraction (PXRD) patterns of MV_2Al_{20} (M = Sc, Y, La, Lu), with a successful structural fit of the data to the $CeCr_2Al_{20}$ structure type, are shown in Fig. 2. The excellent quality of the refinements confirms the high purity of the materials. Only a very small amount of crystalline impurity phases were found in the ScV_2Al_{20}, YV_2Al_{20}, and LaV_2Al_{20} samples. In case of ScV_2Al_{20} and LaV_2Al_{20}, the impurity reflections matched the diffraction profiles of aluminum and Al_3V [57,58], respectively. The impurity phase in YV_2Al_{20} could not be unambiguously identified, but most probable candidates are Al-rich binary vanadium compounds, like $Al_{23}V_4$ or $Al_{45}V_7$ [59]. It is worth noting that the Al-Y system contains an eutectic at approximately 3 at. % Y with a melting temperature of 637 °C, more than 20 °C below melting point of pure Al [60]. This can lead to partial melting of the sample during the annealing process at 650 °C and hence result in poor material homogeneity.

The crystal structure parameters resulting from the Rietveld refinements are gathered in Table I. Refinement of the occupancy factor (SOF) of Sc-, Y-, La-, and Lu-containing samples led to values close to 1 (a stoichiometric composition). The unit cell parameters and the dimensions of the M-Al polyhedra
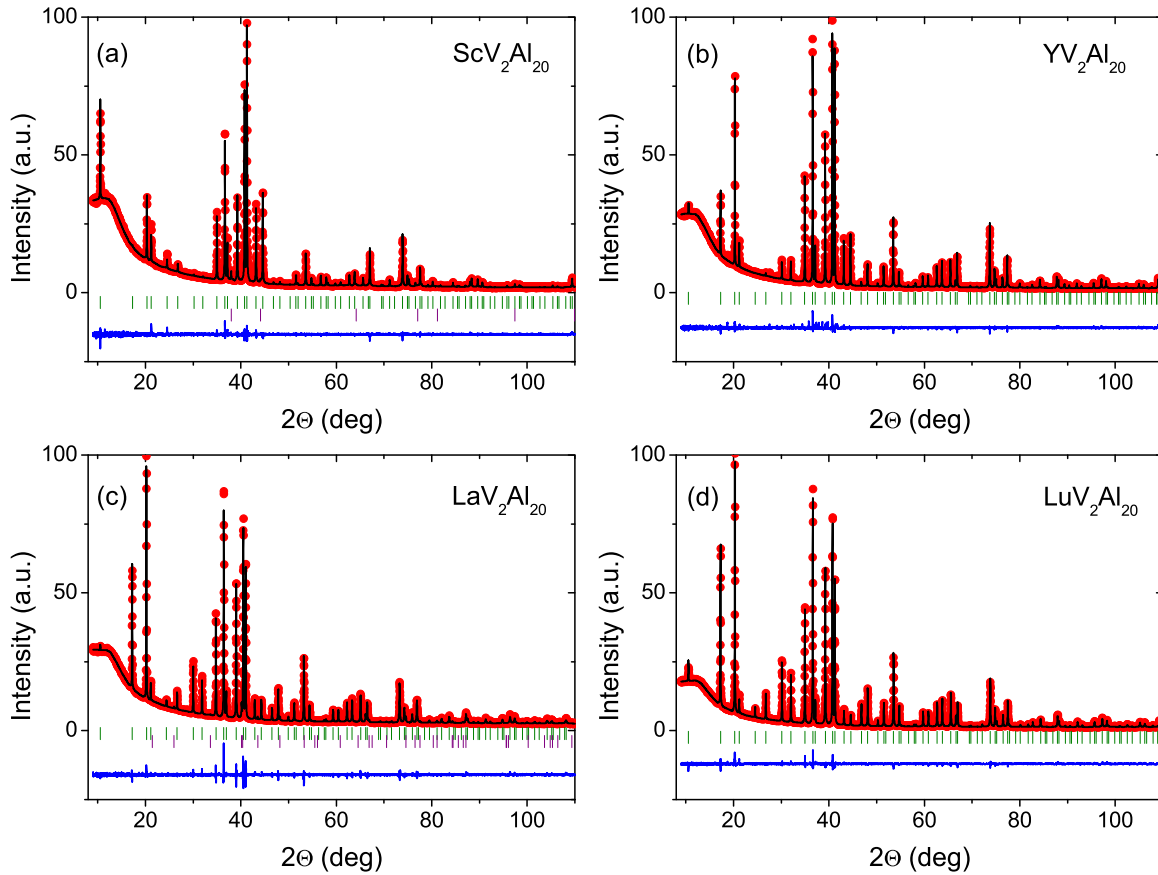
FIG. 2. Rietveld fits to the XRD patterns obtained for (a) ScV_2Al_{20}, (b) YV_2Al_{20}, (c) LaV_2Al_{20}, and (d) LuV_2Al_{20}. Red points—observed intensities (I_{obs}), black line—calculated intensities (I_{calc}), blue line—$I_{obs} - I_{calc}$. Green ticks marks the expected positions of Bragg reflections for the main phase; violet—for the impurity [Al and Al_3V in (a) and (c), respectively]. For the values of Rietveld R factors and crystallographic data derived from fits see Table I.

are summarized in Table II. ScV_2Al_{20} has the smallest cell parameter within the series, although the relative differences between individual compounds do not exceed 1%. The unit cell dimensions of LuV_2Al_{20} are lower than those of LaV_2Al_{20}, which is in agreement with the lanthanide contraction effect.

Figure 3(a) summarizes the unit cell parameters for selected MV$_2$Al$_{20}$ compounds and the values obtained in this study. There is a clear trend visible for the lanthanide series, namely the cubic lattice parameter systematically decreases with decreasing atom size, entirely in line with the lanthanide contraction effect. However, for smaller atoms, including Lu, Sc, Al, and Ga, the unit cell parameter does not change significantly, despite an approximately 50% increase in the covalent radius between Al and Lu. This finding suggests that below a certain atomic radius, the filling atom affects neither the size of the hosting cage nor the unit cell volume. If the dimension of the central atom is larger than the cage size, it causes cage expansion and the unit cell increases. Figure 3(b) shows the apparently linear dependencies of cage filling factors (defined as the ratio of M atom radius and the average M-Al distance as well as the ratio of M atom volume and the cage volume). It is worth mentioning that the Baur distortion index [61], calculated for the icosahedral M-Al cages, also scales with the increasing size of the filling atom.

B. Magnetic properties

The temperature dependencies of the dc molar magnetic susceptibility $\chi_M(T)$ measured down to 0.5 K of ScV_2Al_{20} (a), YV_2Al_{20} (b), and LuV_2Al_{20} (c) are shown in Fig. 4. Measurements were performed after zero-field cooling (ZFC) in an applied magnetic field of 20 Oe (40 Oe in case of YV_2Al_{20}). A sharp diamagnetic drop in the susceptibility (superconducting transition) is observed at 1.0, 0.6, and 0.58 K for ScV_2Al_{20}, YV_2Al_{20}, and LuV_2Al_{20}, respectively. χ_M signal at the lowest achievable temperature ($T = 0.48$ K) is relatively strong and almost identical for all the tested samples. For LaV_2Al_{20} no superconducting transition was found down to 0.5 K, in agreement with the magnetization results reported by Onosaka *et al.* [48]. To further characterize the superconducting state, the magnetization measurements versus applied field $M(H)$ were performed at $T = 0.48$ K. The shapes of $M(H)$ (see Fig. 4) suggest that all three compounds studied are type-II superconductors with the lower critical field $H_{c1}(0.48$ K) below 20 Oe (2 mT).

C. Electrical transport

The temperature dependencies of the normalized resistivity ($\rho/\rho_{300\,K}$) of MV$_2$Al$_{20}$ between 0.4 and 300 K are shown

TABLE I. Crystallographic data obtained from Rietveld refinement of powder x-ray diffraction patterns. Numbers in parentheses indicate the statistical uncertainty of the least significant digit resulting from the fit. Differences in cell parameters between the compounds agree with the differences in covalent radii of the $8a$ atoms.

	ScV_2Al_{20}	YV_2Al_{20}	LaV_2Al_{20}	LuV_2Al_{20}
Space group		*Fd-3m* (# 227)		
Pearson symbol		cF184		
Z (number of formula units per unit cell)		8		
Cell parameter (Å)	14.4978(1)	14.5378(1)	14.6219(5)	14.5130(1)
Cell volume (Å^3)	3047.231	3072.523	3126.162	3056.832
Molar weight (g mol^{-3})	686.4689	730.4189	780.4185	816.4800
Density (g cm^{-3})	2.993	3.158	3.316	3.548
M (8a) $x = y = z$		1/8		
V (16d) $x = y = z$		1/2		
Al1 (16c) $x = y = z$		0		
Al2 (48f) $x =$	0.4873(2)	0.4861(1)	0.4864(2)	0.4860(1)
$y = z =$		1/8		
Al3 (96g) $x = y =$	0.0601(1)	0.0595(1)	0.0588(1)	0.0593(1)
$z =$	0.3238(1)	0.3251(1)	0.3266(1)	0.3245(1)
Figures of merit:				
R_p (%)	27.4	20.8	19.3	12.6
R_{wp} (%)	16.2	14.1	13.5	9.61
R_{expt} (%)	12.32	9.03	7.93	6.14
χ^2 (%)	1.73	2.44	2.88	2.45

in Fig. 5. All samples exhibit metallic conductivity, and the residual resistivity ratio ($RRR = \rho_{300\,K}/\rho_{2\,K}$) varies from

TABLE II. Crystallographic data obtained from the Rietveld refinement. The M-Al cage radius is defined as an average bond length between the M atom (8a position) and surrounding Al atoms. Numbers given in parentheses are uncertainties of the least significant digit(s). Cage distortion indices [61], radii and volumes were calculated using VESTA software [41]. For plot of relative cage sizes and distortion indices vs the 8a atom size see the Supplemental Material [62].

	ScV_2Al_{20}	YV_2Al_{20}	LaV_2Al_{20}	LuV_2Al_{20}
Cell parameter a (Å)	14.4978(1)	14.5378(1)	14.6219(5)	14.5130(1)
M-Al cage radius R_{cage} (Å)	3.1655	3.1908	3.2357	3.1809
M-Al cage volume V_{cage}(Å^3)	91.4167	93.5403	96.7032	92.6832
M-Al cage distortion index (%)	0.421	0.678	0.973	0.609
Covalent radius of M atom r_{atom} (Å) [63]	1.70(7)	1.90(7)	2.07(8)	1.87(8)
r_{atom}/R_{cage} (%)	53.7%	59.5%	64.0%	58.8%
V_{atom}/V_{cage} (%)	22.5%	30.7%	38.4%	29.6%

1.1 (ScV_2Al_{20}) to 12.2 (LaV_2Al_{20}). The almost temperature independent ρ observed for ScV_2Al_{20} may arise due to either substantial scattering at the grain boundaries, or internal inhomogeneity, similar to that often observed for example in Heusler superconductors [67,68], where heat treatment of samples can lead to enhanced antisite disorder. The second scenario is supported by the fact that the RRR increases
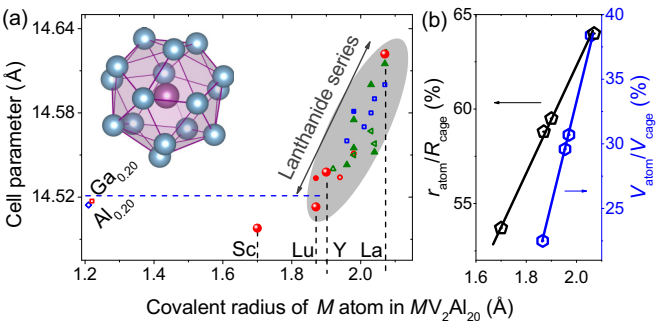

FIG. 3. (a) Dependence of unit cell parameter a of selected MV_2Al_{20} [27,42,64,65] based on the covalent radius of M atom [63], r_{atom}. For lanthanide atoms, a linear relation between a and r_{atom} is observed, whereas for smaller Al, Ga, Sc, and Lu atoms, cell parameters do not vary significantly, despite about 50% increase in the r_{atom} between Al and Lu. Inset shows the M(8a)-Al(96g, 16c) cage. (b) A plot of filling factor (see text) dependencies on the r_{atom} for MV_2Al_{20} (M = Sc, Y, La, and Lu) compounds synthesized in this work. Both the radii (black) and volume ratios (blue) show a linear relation with r_{atom} (solid lines are guide to eyes). For full version of the plot (a) with additional data and references see Supplemental Material [66].
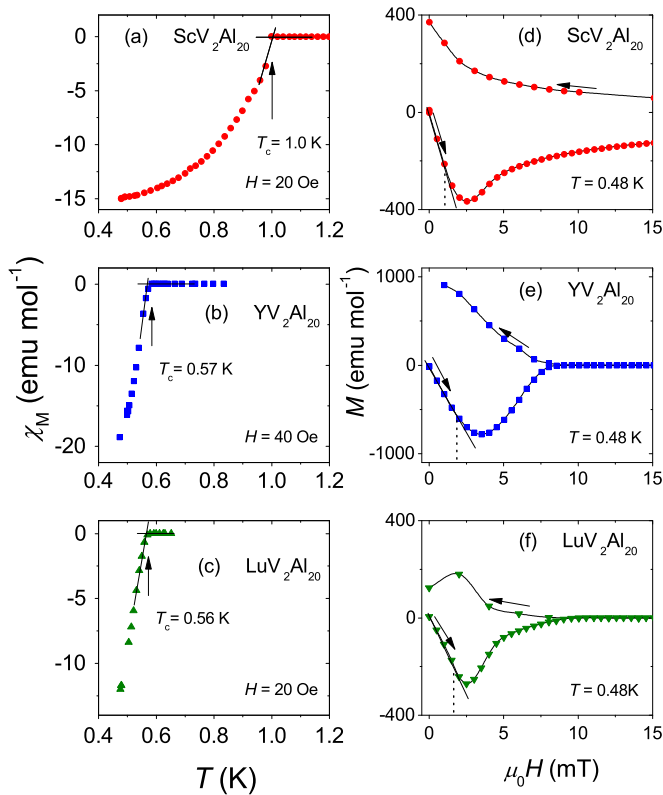
FIG. 4. (a)–(c) Temperature dependence of the zero-field cooled, molar magnetic susceptibility (χ_M) in the vicinity of the superconducting transition for (a) ScV$_2$Al$_{20}$, (b) YV$_2$Al$_{20}$, and (c) LuV$_2$Al$_{20}$. (d)–(f) Molar magnetization (M) versus applied magnetic field (H) measured at $T = 0.48$ K for (d) ScV$_2$Al$_{20}$, (e) YV$_2$Al$_{20}$, and (f) LuV$_2$Al$_{20}$.

with increasing a covalent radius of the rare earth metal M. Scandium is the smallest rare earth metal and due to its comparable size with vanadium, an intermixing effect in ScV$_2$Al$_{20}$ seems likely. It is worth noting that Lortz *et al.* reported that the *RRR* value for Ba$_8$Si$_{46}$ sample (with much higher T_c) was significantly lower than for Ba$_{24}$Si$_{100}$ [20].
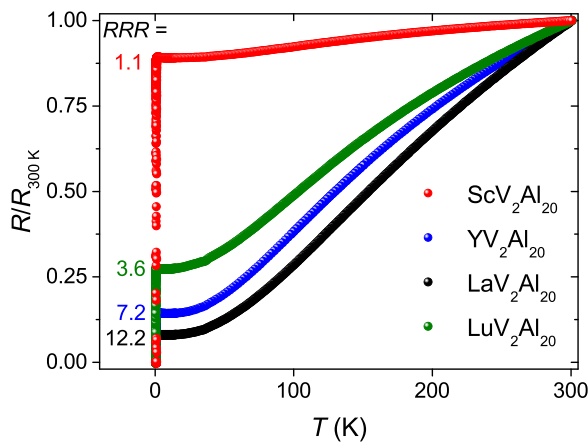

FIG. 5. Relative resistivity [$R(T)/R(300$ K)] vs temperature plots for all four materials synthesized in this study. The RRR ratios [$R(300$ K)/$R(2$ K)] vary from 1.1 (ScV$_2$Al$_{20}$) to 12.2 (LaV$_2$Al$_{20}$).

Figure 6 shows the low-temperature electrical resistivity data of ScV$_2$Al$_{20}$, YV$_2$Al$_{20}$, LaV$_2$Al$_{20}$, and LuV$_2$Al$_{20}$, measured in zero and finite external magnetic fields. For ScV$_2$Al$_{20}$, YV$_2$Al$_{20}$, and LuV$_2$Al$_{20}$ a resistivity drop to zero was observed, in contrast to LaV$_2$Al$_{20}$. The superconducting critical temperatures, estimated as the midpoint of the transitions, are 1.03, 0.61, and 0.60 K for the three compounds, respectively. These values are in very good agreement with the T_c values estimated from the magnetic susceptibility data. The double superconducting transition for YV$_2$Al$_{20}$ that is seen for $H > 50$ Oe, suggests the presence of a second superconducting phase with a different upper critical field.

Figure 7 presents the temperature dependence of the upper critical field for MV$_2$Al$_{20}$, with the data points obtained from the resistivity measurements. The initial slope dH_{c2}/dT_c can be used to estimate the upper critical field $H_{c2}(0)$ using the Werthamer-Helfand-Hohenberg (WHH) expression for a dirty-limit superconductor [69]:

$$H_{c2}(0) = -0.69 \cdot T_c \left(\frac{dH_{c2}}{dT} \right) \bigg|_{T=T_c}. \quad (1)$$

Taking T_c obtained from the resistivity measurements, one finds $\mu_0 H_{c2}(0) = 0.33$, 0.03, and 0.21 T for ScV$_2$Al$_{20}$, YV$_2$Al$_{20}$, and LuV$_2$Al$_{20}$, respectively.

Given the zero-temperature upper critical field $\mu_0 H_{c2}(0)$, the Ginzburg-Landau coherence length ξ_{GL} can be calculated using the formula

$$\mu_0 H_{c2} = \frac{\varphi_0}{2\pi \xi_{GL}^2}, \quad (2)$$

where φ_0 is the quantum of magnetic flux. Estimated values of ξ_{GL} are 314, 1084, and 399 Å for Sc-, Y-, and Lu-containing samples, respectively.

D. Heat capacity

The results of heat capacity measurements for the three superconducting compounds MV$_2$Al$_{20}$ (M = Sc, Y, Lu) are shown in Fig. 8. Bulk nature of the superconductivity and good quality of the tested samples are confirmed by sharp anomalies observed at 1, 0.6, and 0.57 K for ScV$_2$Al$_{20}$, YV$_2$Al$_{20}$, and LuV$_2$Al$_{20}$, respectively. The solid lines through data points represent the entropy-conservation construction, and the superconducting temperatures were estimated as a midpoint of the transition. Figures 8(d)–8(f) show the variation of C_p/T with T^2 at zero magnetic field above the superconducting transition. The data points were fitted using the formula $\frac{C_p}{T} = \gamma + \beta T^2 + \delta T^4$ to determine the Sommerfeld coefficient γ and phonon heat capacity coefficients β and δ. The fits give similar γ values between 26.5(2) mJ mol^{-1} K^{-2} (YV$_2$Al$_{20}$) and 30.1(1) mJ mol^{-1} K^{-2} (ScV$_2$Al$_{20}$). Knowing γ one can calculate the normalized heat capacity jump $\Delta C/\gamma T_c$, which characterizes the electron-phonon coupling. For ScV$_2$Al$_{20}$ and LuV$_2$Al$_{20}$, the estimated $\Delta C/\gamma T_c = 1.47$ and 1.36 are close to the BCS value (1.43) for a weakly coupled superconductor. The significantly lower $\Delta C/\gamma T_c = 1.23$ obtained for YV$_2$Al$_{20}$ is likely caused by the presence of impurity phases. This is in agreement with the XRD results, preliminary SEM+EDS microscopic studies, and the resistivity data. The upper critical
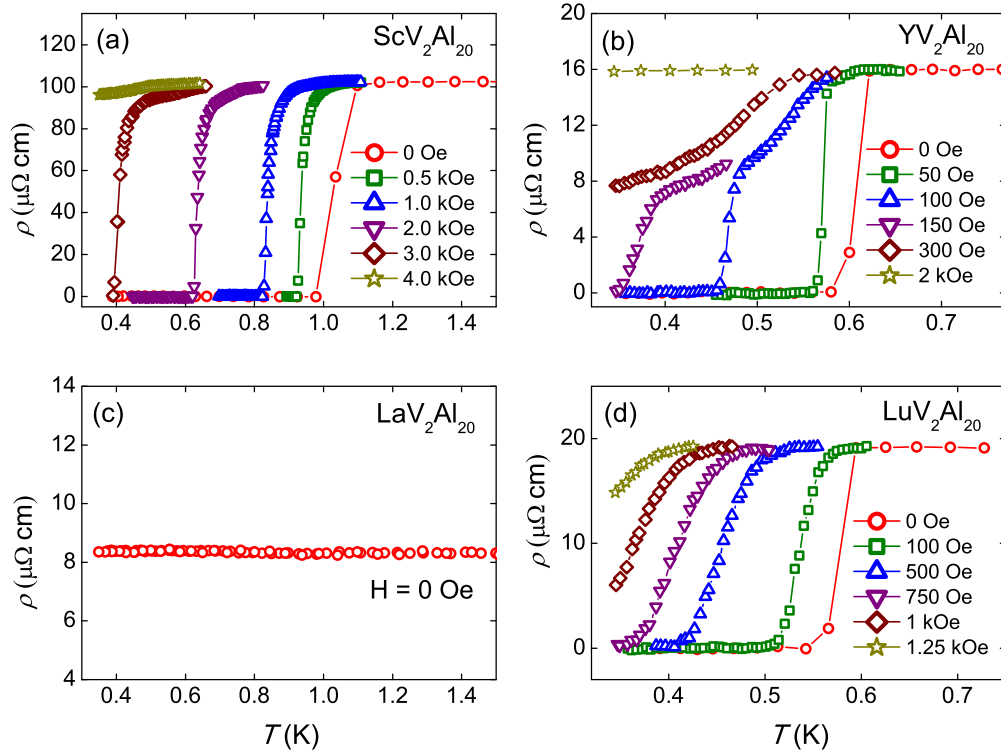
FIG. 6. Plots of the low-temperature region of the resistivity data showing the drop to 0 at T_c for (a) ScV_2Al_{20}, (b) YV_2Al_{20}, and (d) LuV_2Al_{20}. No superconducting transition was observed in case of (c) LaV_2Al_{20}. The double transition seen in (b) suggests the presence of material inhomogeneity.

field determined for ScV_2Al_{20} and LuV_2Al_{20} amounts to approximately 0.3 and 0.2 T, respectively, while $\mu_0 H_{c2}(0)$ found for YV_2Al_{20} is smaller by an order of magnitude.

In a simple Debye model, the β coefficient is related to the Debye temperature Θ_D through the relation

$$\Theta_D = \sqrt[3]{\frac{12\pi^4 n R}{5\beta}}, \qquad (3)$$

where n is the number of atoms per formula unit and R is the gas constant. Although the Debye model is rather poorly applicable for complex intermetallics (see phonon computations results in the next section), it was applied here as a standard description of the physical properties of MV_2Al_{20} compounds. The so-obtained Debye temperatures fall in the range of approximately 500 K, and thus are higher than the Debye temperature for pure Al ($\Theta_D = 428$ K). The highest value of $\Theta_D = 536(8)$ K was found for ScV_2Al_{20} that bears the lightest M element, and the lowest value of $\Theta_D = 502(5)$ K was obtained for the heaviest LuV_2Al_{20}, as expected. This simple reasoning, however, does not apply to YV_2Al_{20} and LaV_2Al_{20} [$\Theta_D = 516(8)$ and $525(8)$ K, respectively].

The observed departures from $C_{lattice} \sim T^3$ behavior [see Figs. 8(d) and 8(f)] signal that the density of low frequency phonon states does not follow the ω^2 law that is assumed in the Debye model. In most cases, at temperatures below $\Theta_D/50$ the deviation from the ω^2 law is negligible, thus δT^4 and higher terms of the Debye heat capacity expansion are significant only at higher temperatures, between approximately $\Theta_D/50$ and $\Theta_D/10$ [70]. Values of the δ heat capacity coefficient obtained

for LaV_2Al_{20} and YV_2Al_{20} are an order of magnitude lower than those derived for ScV_2Al_{20} and LuV_2Al_{20}. In the former two compounds the $\sim T^2$ dependency between C_p/T and T^2 holds up to 10 K ($\sim\Theta_D/50$) in contrast with the latter ones, where deviation from a linear behavior is clearly visible above ~ 5 K. This shows that in case of ScV_2Al_{20} and LuV_2Al_{20} the deviations of the low frequency phonon density of states from the Debye-like shape should be significantly stronger, which was indeed clearly seen in the results of theoretical calculations (see next section). It is worth mentioning that the $C_{lattice} \sim T^5$ dependence in low temperatures was previously found in β-pyrochlores [1,16].

Given the critical temperature T_c, the Debye temperature Θ_D, and assuming the Coulomb pseudopotential parameter $\mu^\star = 0.13$, the electron-phonon coupling constant can be calculated using the modified McMillan's formula [72]:

$$\lambda_{el-ph} = \frac{1.04 + \mu^* \ln\left(\frac{\Theta_D}{1.45 T_c}\right)}{(1 - 0.62\mu^*) \ln\left(\frac{\Theta_D}{1.45 T_c}\right) - 1.04}. \qquad (4)$$

The obtained λ_{el-ph} constant is almost identical for the all three superconducting compounds: $\lambda_{el-ph} = 0.45$ for ScV_2Al_{20} and 0.42 for YV_2Al_{20} and LuV_2Al_{20}. These values of λ_{el-ph} indicate that the studied compounds are weak-coupling super-conductors.

The measured and calculated thermodynamic characteristics of the MV_2Al_{20} ($M =$ Sc, Y, Lu, La) compounds are summarized in Table III. The critical temperature of YV_2Al_{20} obtained from the analysis of the heat capacity jump (0.60 K) is slightly lower than the previously reported value of 0.69 K, also based on C_p measurements [44]. The discrepancy can be
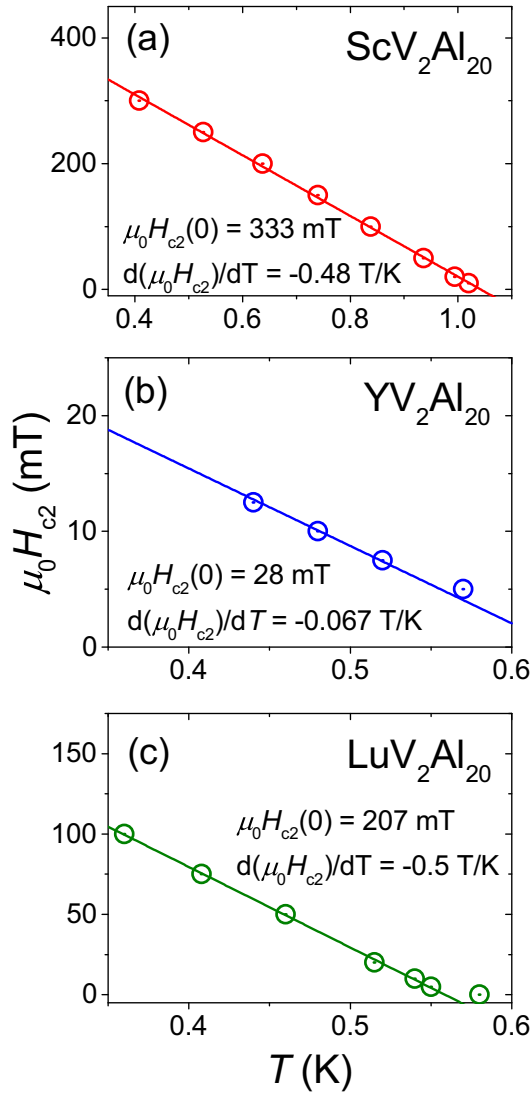
FIG. 7. The dependence of the upper critical field on temperature for (a) ScV_2Al_{20}, (b) YV_2Al_{20}, and LuV_2Al_{20}. Solid lines are linear fits to the experimental data. The values of $\mu_0 H_{c2}(0)$ were calculated using the WHH expression (see text).

FIG. 8. Plots of the low-temperature part of heat capacity measurements for (a) ScV_2Al_{20}, (b) YV_2Al_{20}, and (c) LuV_2Al_{20}, showing the anomalies due to the superconducting transition. Superconducting critical temperatures were estimated using the entropy conserving construction (black solid lines). (d)–(f) The fits (black solid lines) to the low temperature heat capacity results above the superconducting transition obtained at zero magnetic fields. C_p/T vs T^2 curves for YV_2Al_{20} (e) and LaV_2Al_{20} (not shown) show a linear character up to 10 K ($\sim\Theta_D/50$), whereas for the cases of ScV_2Al_{20} (d) and LuV_2Al_{20} (f) a clear quadratic dependence is clearly visible above approximately 5 K. Gray dashed lines (d) and (f) are added to emphasize the deviation from linearity. Plots shown on (d)–(f) are compared with the data for LaV_2Al_{20} in the Supplemental Material [71].

explained as a higher sample quality synthesized by Onosaka *et al.* [44] (likely caused by a different heat-treatment method), which is also reflected by a lower value of $\frac{\Delta C_p}{\gamma T_c}$ (1.24, compared to 1.41 in Ref. [44]). The obtained values of the Sommerfeld coefficient in YV_2Al_{20}, LaV_2Al_{20}, and LuV_2Al_{20} are in good agreement with the previous results [48].

IV. THEORETICAL STUDIES

To analyze the superconductivity mechanism in MV$_2$Al$_{20}$, density functional theory (DFT) electronic structure and phonon calculations were undertaken. As the starting point, calculations for the experimental crystal structures of the studied materials were performed using the full potential linearized augmented plane wave (FP-LAPW) method, as implemented in the WIEN2K code [73]. The Perdew-Burke-Ernzerhof generalized gradient approximation [74] (PBE-GGA) was used for the exchange-correlation potential, computations were done on
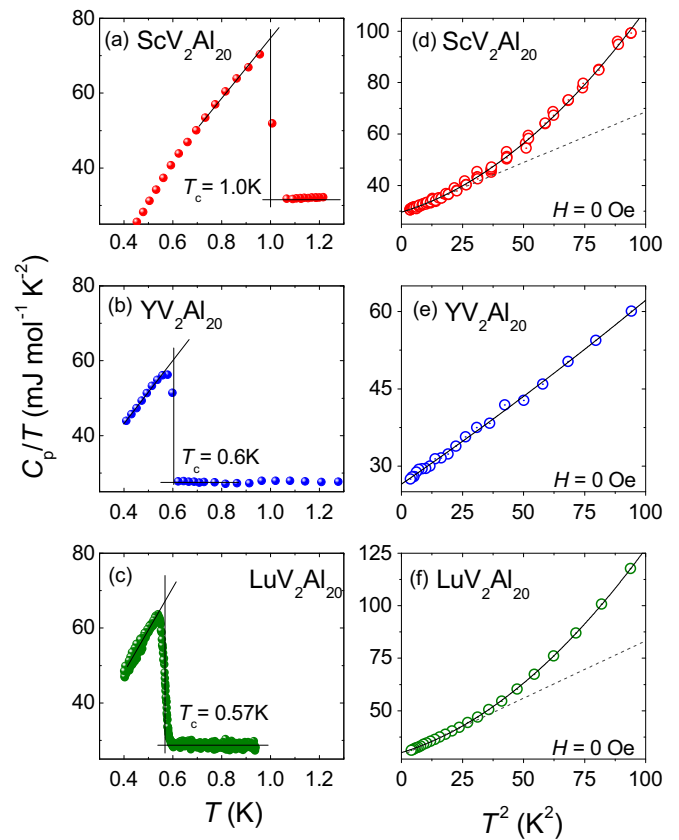
a $10\times10\times10$ k-point mesh and included the spin-orbit (SO) coupling. Comparison with the semirelativistic computations showed, that even for the case of heavy M elements (La, Lu), SO interaction does not modify the density of states (DOS) near the Fermi level. The total and partial atomic densities of states are gathered in Fig. 9. The overall shapes of the DOS curves are very similar in the series of compounds, which is expected due to their isoelectronic character. For the La- and Lu-containing materials, large DOS peaks due to the $4f$ electron shells can be easily identified [see Figs. 9(c) and 9(d)]. In LaV_2Al_{20}, the empty $4f$ La states are located 3 eV above E_F, whereas in LuV_2Al_{20} the DOS structure of the filled $4f$ shell of Lu, additionally split by the spin-orbit interaction, is located 5–6 eV below E_F.

It is worth noting that the envelopes of the DOS curves for the lower energies are similar to the DOS curves of metallic fcc

TABLE III. Parameters of the superconducting state estimated from heat capacity, magnetization, and resistivity measurements. Numbers in parentheses indicate the uncertainty of the least significant digit(s).

	Sc	Y	Lu	La
γ (mJ mol^{-1} K^{-2})	29.6(2)	26.5(2)	30.1(1)	19.6(2)
β (mJ mol^{-1} K^{-4})	0.29(1)	0.32(1)	0.35(1)	0.31(1)
Θ_D (K)	536(8)	516(8)	502(5)	525(8)
δ (μJ mol^{-1} K^{-6})	4.96(14)	0.33(16)	6.19(13)	0.64(16)
T_c (K)	1.00	0.60	0.57	
$\lambda_{\text{el-ph}}$	0.41	0.39	0.39	
$\frac{\Delta C_p}{T_c}$ (mJ mol^{-1} K^{-2})	43.3	32.8	38.8	
$\frac{\Delta C_p}{\gamma T_c}$	1.46	1.24	1.29	
$\frac{d\mu_0 H_{c2}}{dT_c}$ (T K^{-1})	$-0.482(6)$	$-0.067(5)$	$-0.501(6)$	
$\mu_0 H_{c2}(0)$ (T)	0.333(4)	0.028(2)	0.207(2)	
ξ_{GL} (Å)	314(2)	1084(39)	399(2)	

aluminum, additionally plotted in the figures for convenient comparison (DOS of fcc Al is multiplied by 23 that is the number of atoms per f.u. in the MV$_2$Al$_{20}$). The significant differences start above -3 eV, where the partial DOS curves

due to the M and V elements show up. This similarity might suggest that the electronic structure of MV$_2$Al$_{20}$ may be quite similar to the electronic structure of the (hypothetical) fcc M-V-Al random alloy. This supposition, however, occurred not to be true, as was verified for the M = Sc example, for which additional calculations by the KKR-CPA method [75] were performed. The DOS of the random Sc-V-Al alloy is given in the inset of Fig. 9(a) and is significantly different from that of ScV$_2$Al$_{20}$. For the random alloy case, energetically unfavorable broad maximum in DOS is observed near the Fermi level, instead of a deep minimum that likely stabilizes the ordered compound.

DOS curves, expanded near the Fermi level, are presented in Fig. 10, and the corresponding values of the total DOS at E_F, $N(E_F)$, are shown in Table IV. In spite of the differences in the shape of DOS near E_F, YV$_2$Al$_{20}$, LaV$_2$Al$_{20}$, and LuV$_2$Al$_{20}$ have almost equal $N(E_F) \approx 8$ eV^{-1} (per f.u.). This similarity contradicts with the experimentally observed superconducting properties, where M = Y, Lu have nearly equal $T_c = 0.6$ K, whereas the La-containing compound is not superconducting down to 0.4 K. In turn, ScV$_2$Al$_{20}$ exhibits the highest DOS value $N(E_F) = 9.0$ eV^{-1}, which is correlated with the highest T_c within the series.

The combination of the experimentally measured electronic heat capacity coefficient γ_{expt} with the theoretically calculated $\gamma_{\text{calc}} = \frac{\pi^2}{3} k_B^2 N(E_F)$ allows us to estimate the value of
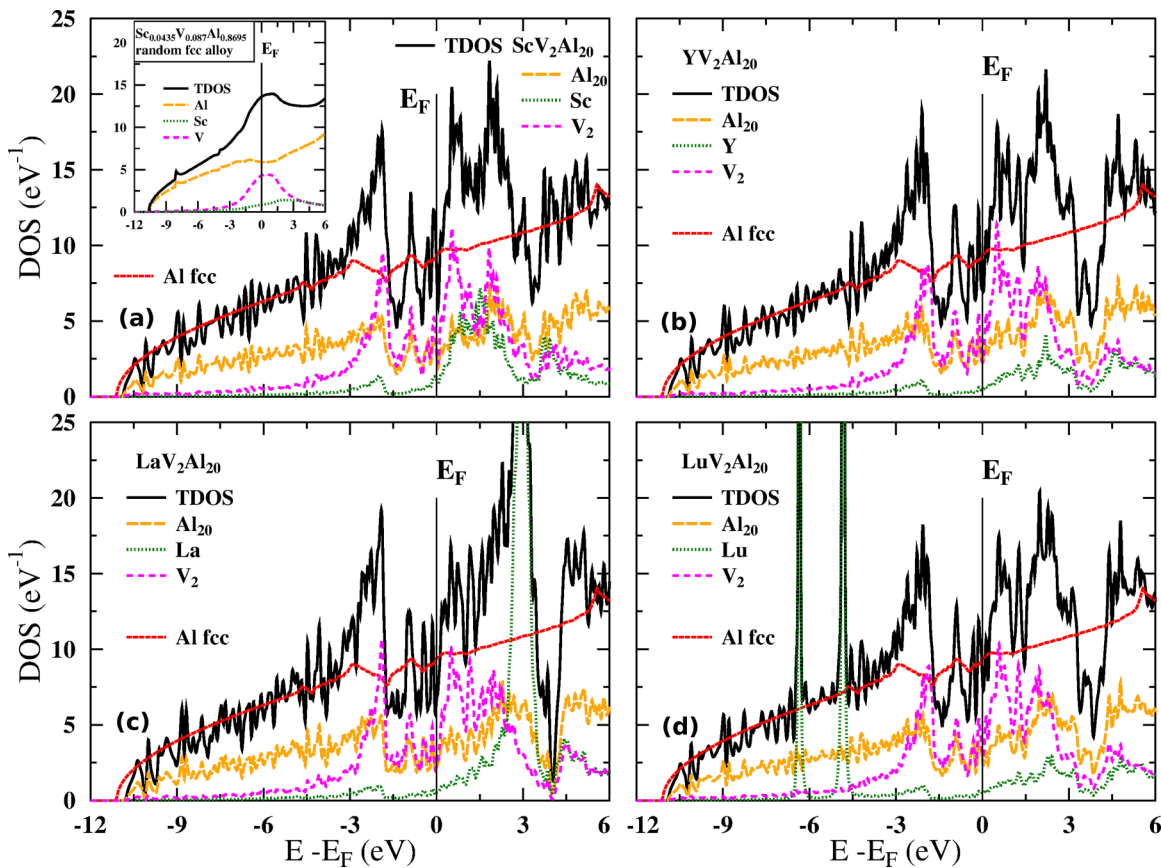

FIG. 9. Densities of states (DOS) of the MV$_2$Al$_{20}$ compounds. TDOS is the total DOS per formula unit, color lines mark contributions from each group of the atoms in the unit cell (summed over all positions). The inset in (a) shows DOS of the random Sc-V-Al alloy, having equivalent composition to the ScV$_2$Al$_{20}$ compound (see the text).
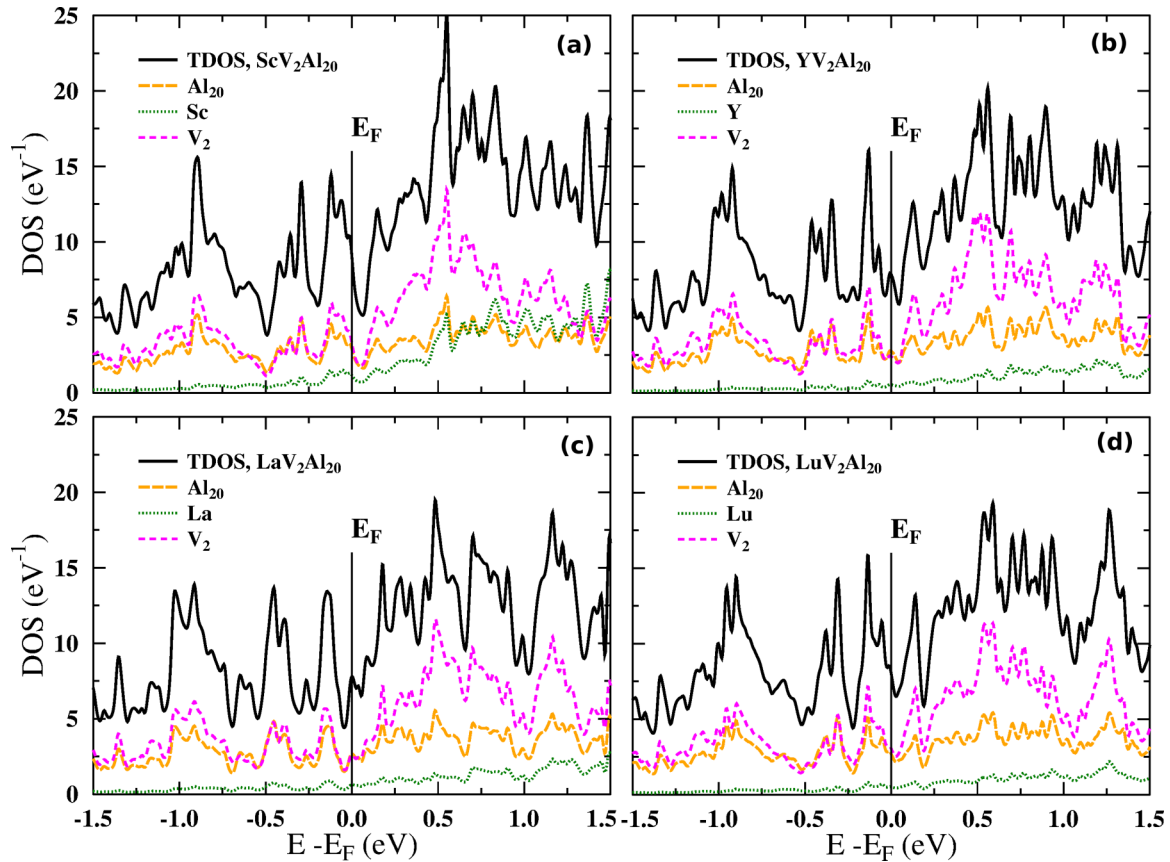
FIG. 10. Densities of states (DOS) of the MV$_2$Al$_{20}$ compounds near the Fermi level. TDOS is the total DOS per formula unit, color lines mark contributions from each group of the atoms in the unit cell (summed over all positions).

the electron-phonon coupling parameter $\lambda_{\text{el-ph}}$ from the relationship $\gamma_{\text{expt}} = \gamma_{\text{calc}}(1 + \lambda_{\text{el-ph}})$. The computed values are presented in Table IV. For LaV$_2$Al$_{20}$, a very weak electron-phonon interaction $\lambda = 0.03$ was found, in line with nonsuperconducting behavior of this compound down to the lowest temperatures. The other three compounds exhibit $\lambda_{\text{el-ph}}$ in the range $\lambda_{\text{el-ph}} = 0.40$–$0.59$, and generally the estimation based on γ agrees with the estimation based on T_c and McMillan formula (cf. values in Tables III and IV), with the largest difference for the $M = $ Lu case [$\lambda_{\text{el-ph}} = 0.42$ from T_c versus $\lambda_{\text{el-ph}} = 0.59$ from $N(E_F)$ and γ].

To understand the differences in the λ and particularly the weak electron-phonon interaction in the La-bearing compound, further computations were carried out. The electronic contributions to λ, i.e., the McMillan-Hopfield parameters η

[72,76], were obtained within the rigid muffin tin approximation (RMTA) [77–79] and KKR formalism [75] in the semirelativistic approach. The parameters η_i of each atom in the unit cell enter the approximate formula for the electron-phonon coupling constant:

$$\lambda_{\text{el-ph}} = \sum_i \frac{\eta_i}{M_i \langle \omega_i^2 \rangle}, \tag{5}$$

where $\langle \omega_i^2 \rangle = \int \omega F_i(\omega)d\omega / \int \omega^{-1} F_i(\omega)d\omega$ is the "average square" phonon frequency of the atom i with atomic mass M_i, while F_i stands for the partial phonon DOS. These formulas and the RMTA approach are based on several strong assumptions (see, e.g., Refs. [78,79]), which may not be satisfied in such complicated cage compounds (see below). The computed η_i parameters are presented in Table V, where each of the value is given per one atom, located at its crystal site in the primitive cell. Populations of each site in the primitive cell are 2 (M), 4 (V), 24 (Al(96g)), 12 (Al(48f)), and 4 (Al(16c)) (which is 1/4 of the site number, since the unit cell is of a face-centered type). First, it can be seen that the nonsuperconducting LaV$_2$Al$_{20}$ compound has the lowest η_i values on all of the constituent atoms, while compared to the other three systems. The Al atoms at each of the sites exhibit similar values among the different compounds, and, due to the large population of the site, the Al(96g) atom will be more important for the superconductivity than Al(48f) and Al(16c). Variation in the values of η_i at the V atom is moderate, with the

TABLE IV. Calculated total densities of states at the Fermi level $N(E_F)$ per formula unit, for the MV$_2$Al$_{20}$ compounds, corresponding Sommerfeld electronic heat capacity coefficients γ_{calc}, and electron-phonon coupling constant, derived from the comparison of the calculated and experimental (γ_{expt}) Sommerfeld parameters.

M	Sc	Y	La	Lu
$N(E_F)$ (eV^{-1}) per f.u.	9.00	7.85	8.05	8.03
γ_{calc} (mJ mol^{-1} K^{-2})	21.2	18.5	19.0	18.9
$\lambda_{\text{el-ph}} = \gamma_{\text{expt}}/\gamma_{\text{calc}} - 1$	0.40	0.43	0.03	0.59

TABLE V. Computed McMillan-Hopfield parameters, η_i in mRy/a_B^2, given per one atom in the primitive cell (which contains two formula units, i.e., 46 atoms). Experimental T_c is repeated after Table III for convenience. All atoms are labeled with their corresponding crystal sites, the population of the site in the primitive cell is 1/4 of the site number.

			$\eta_i(mRy/a_B^2)$			
M	$M(8a)$	V($16d$)	Al($96g$)	Al($48f$)	Al($16c$)	T_c expt.
Sc	1.94	3.34	0.18	0.27	0.08	1.00
Y	1.53	3.32	0.18	0.28	0.08	0.60
La	0.86	2.74	0.15	0.23	0.06	
Lu	1.26	3.52	0.18	0.27	0.07	0.57

smallest one seen for the LaV$_2$Al$_{20}$ case. The largest dispersion in η_i is seen for the M atoms, with the value for Sc being the highest, and that for La the lowest, more than two times smaller than that for Sc. These trends in η_i well correspond with the measured superconducting critical temperatures. One of the reasons for the differences in the McMillan-Hopfield parameters among the isoelectronic series of M elements comes from the relative amount of the partial d-like DOS at the Fermi level. Scandium, as the early $3d$ element, has the largest value ($\sim 1\,eV^{-1}$ from KKR), which is next decreasing for Y and Lu (both around $0.5\,eV^{-1}$), and reaching $\sim 0.3\,eV^{-1}$ for La, in the same order as the experimental T_c value changes. The other factor, also scaling in the same way, is the lattice parameter and the cage filling factor of the MV$_2$Al$_{20}$, namely the smallest values are observed in ScV$_2$Al$_{20}$, similar for the compounds with Y and Lu, and the largest values for LaV$_2$Al$_{20}$. Since the McMillan-Hopfield parameters typically decrease with the increasing volume of the system (see, e.g., Refs. [80,81]) this trend is reflected in the presented results, at least for the border cases of Sc- and La-bearing materials.

In order to perform the quantitative analysis of the electron-phonon coupling parameter and to probe the impact of atoms filling a cage on the dynamical properties of studied compounds, phonon calculations were next performed. First-principles calculations were done using the projector-augmented wave formalism of the Kohn-Sham DFT within the generalized gradient approximation (GGA) approach in PAW-PBE form, implemented in the Vienna *ab initio* simulation package (VASP) [74,82,83]. The method of Methfessel-Paxton broadening technique with the standard 0.2 eV width of the smearing was adopted to describe the partial occupancies for each wave function. All calculations presented in this study were performed with a crystallographic unit cell consisting of 184 atoms. A k mesh of (2,2,2) points in the Monkhorst-Pack scheme was used for the integration in reciprocal space and the energy cutoff for the plane wave expansion of 400 eV were applied. The crystal structure was optimized using the conjugate gradient technique with the energy convergence criteria set at 10^{-7} and 10^{-5} eV for the electronic and ionic iterations, respectively. The calculated lattice constants and the position of atoms are in very good agreement with the measured parameters, and are shown in Table VI. The atomic positions of M (1/8,1/8,1/8), V(1/2,1/2,1/2), and Al($16c$)(0,0,0) were kept fixed because of the crystal symmetry.

TABLE VI. Relaxed crystal structures data. For experimental values see Table I.

M	Sc	Y	La	Lu
Lattice constants (Å)	14.4391	14.5092	14.5910	14.4816
		Atomic positions		
Al ($96g$)				
$x = y$	0.0560	0.0590	0.0585	0.0593
z	0.3239	0.3251	0.3263	0.3245
Al ($48f$)				
x	0.4856	0.4863	0.4871	0.4859
$y = z$	1/8	1/8	1/8	1/8
Al ($16c$)				
$x = y = z$	0	0	0	0
V ($16d$)				
$x = y = z$	1/2	1/2	1/2	1/2
M ($8a$)				
$x = y = z$	1/8	1/8	1/8	1/8

The vibrational properties of the compounds were calculated using the direct force constant approach implemented in the program PHONON [84,85]. The force constants estimated from the first-principle calculations of Hellmann-Feynman forces are used to build dynamical matrix of crystals. The phonon frequencies were obtained from the diagonalization of the dynamical matrix. In Fig. 11 the total and partial phonon
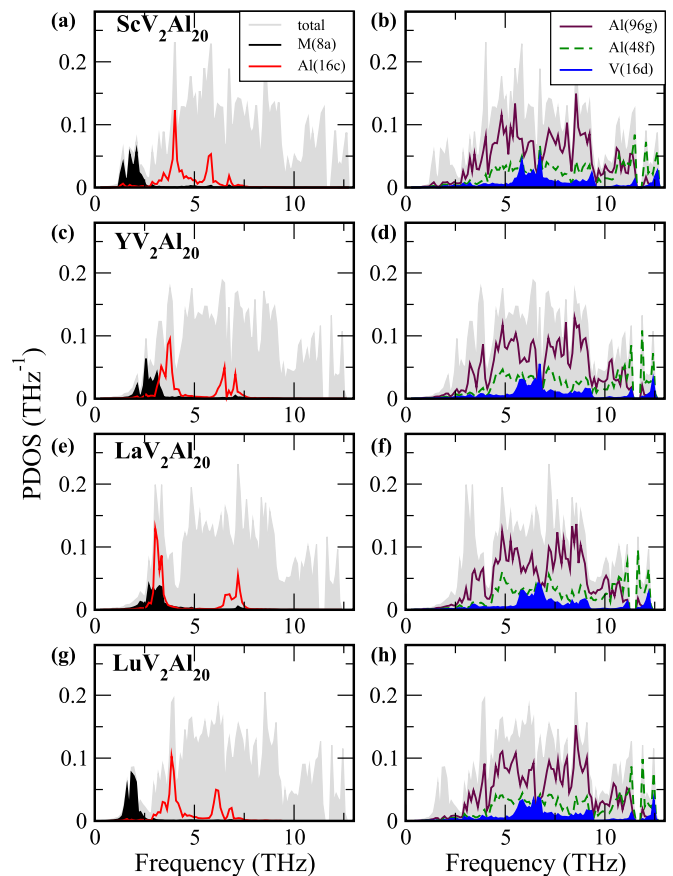

FIG. 11. The total and partial phonon density of states calculated for MV$_2$Al$_{20}$ (M = Sc, Y, La, Lu).

density of states (PDOS) spectra calculated by the random sampling of the first Brillouin zone at 12 000 points are presented. The total PDOS spectra cover the same frequency range up to 13 THz, and the essential differences are present at low frequencies only. For all the investigated compounds the Al(96g), Al(48f), and V(16d) partial PDOS spectra, extended on the whole frequency range, do not differ significantly. The main disparities are observed between the particular vibrational spectra of M(8a) atoms and to a lesser extent by the lowest Al(16c) optic modes. The Al(16c) spectra are characterized by well defined frequencies localized below 7.5 THz, and the positions of the partial PDOS peaks fairly similar for YV$_2$Al$_{20}$ and LuV$_2$Al$_{20}$, essentially differ when compared to ScV$_2$Al$_{20}$ and LaV$_2$Al$_{20}$.The lowest Al(16c) optic mode of LaV$_2$Al$_{20}$ almost covers the frequency range of the La atom vibrations indicating the possible strong interaction between them. For YV$_2$Al$_{20}$, the overlapping of Y and Al(16c) modes is much smaller. Finally, the Sc and Lu vibrations are explicitly localized at the frequency range of acoustic modes. Thus one of the requirements imposed on rattling modes is fulfilled. Remarkably, such localized modes would have to be included to the heat capacity calculated from the Debye model, as additional Einstein modes (see below). The obtained data agree well with the experimental and theoretical results reported for ScV$_2$Al$_{20}$ and LaV$_2$Al$_{20}$ in Ref. [50], and YV$_2$Al$_{20}$ in Ref. [51].

The second requirement of rattling vibrations is their anharmonicity. In the figure of the dispersion relations (Fig. 12) the optical vibrations of the M atoms are presented as almost dispersionless phonon modes lying in the range of the acoustic modes, around 2 THz in the case of Sc- and Lu-bearing compounds or for the lowest optic modes, around 3 THz, for Y and La ones. The M atom contribution to the low-frequency modes is reflected by the partial PDOS (the middle panels of Fig. 12). In the right panels, the phonon dispersion curves calculated using three different displacements of M atoms are presented in the narrow frequency range, depicted by the dashed lines in the middle panels. One can see that the frequencies of a particular vibration depend on the amplitude of the M atom displacement, indicating the anharmonic character of those modes. This anharmonicity is the strongest for M = Sc case, becomes weaker for Y and Lu, and is almost invisible for M = La compound. At Γ point only two modes, T_{1u} and T_{2g}, are anharmonic and both mainly consist of the M atom oscillations, the highest amplitudes of remaining atoms movements are more than an order of magnitude smaller. Moreover, in T_{2g} mode, no oscillations of the V and Al(16c) atoms is observed. The frequency dependence of T_{1u} and T_{2g} on the M atoms' displacement is presented in Table VII.

Analyzing the frequency of T_{2g} mode, calculated for two smaller displacements, the highest changes between frequencies are found for Sc (2.7%). For Y and Lu the differences are considerably smaller (0.7% and 0.5%, respectively) and for La it achieves only 0.1%. It is important to point that the deviation from the harmonic oscillations related to so small displacements cannot be the quasiharmonic effects observed at high temperatures. To verify the character of this mode's anharmonicity, the T_{2g} mode potential energy as a function of mode amplitude Q was also calculated (Fig. 13). The polarization vector of the mode allows us to generate a displacement pattern corresponding to the frozen phonon. The
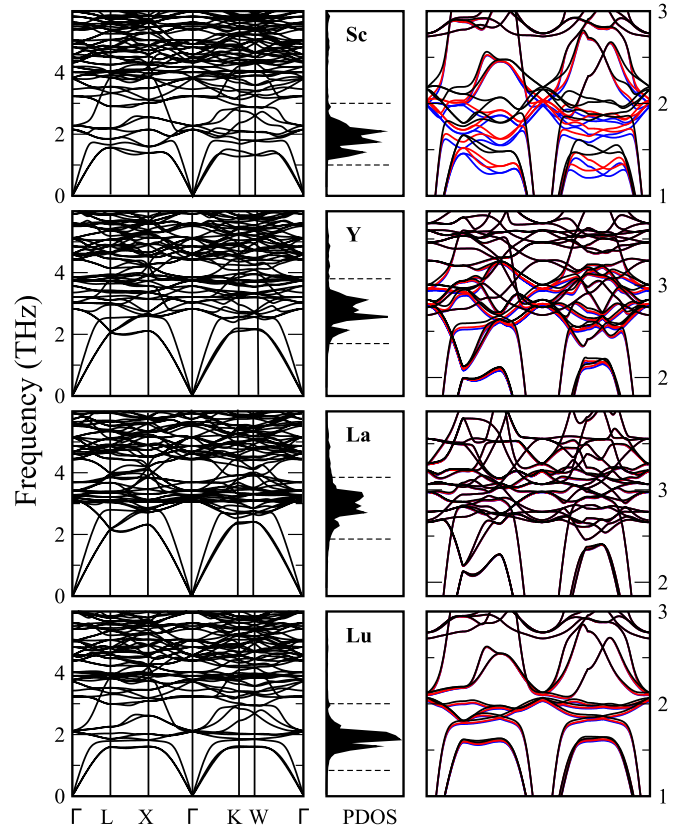

FIG. 12. Left panels: phonon dispersion curves calculated for MV$_2$Al$_{20}$ (M = Sc, Y, La, Lu). Middle panels: the contribution of the M atoms to the phonon density of states. The dashed lines define the frequency range used in the right panels. Right panels: the dispersion curves calculated for three different displacements of M atoms: 0.04 Å (blue), 0.07 Å (red), and 0.14 Å (black) presented in the frequency range of the M atoms vibrations.

magnitude of each atom displacement u_i in a particular mode is proportional to $Q/\sqrt{m_i}$ (m_i = mass of atom), e.g., the mode amplitude $Q = 14$ corresponds to the M atom displacements equal 0.041, 0.025, 0.013, and 0.018 Å for Sc, Y, La, and Lu. In the left panel of Fig. 13, the calculated points are presented together with two polynomial fits, purely harmonic function and harmonic with added quartic term, represented by solid and dashed lines, respectively. In the inset, the data in a whole amplitudes range, used in the fitting procedure, are presented. For Sc, the potential, flat at the bottom, strongly deviates from the quadratic function. For Y and Lu the difference is not so evident. However, comparing two fits to the calculated data, the slight sign of broadening of calculated points is demonstrable, and the fits with the quartic terms are better. The T_{2g} mode potential of La is purely harmonic. The flat potential, especially seen for the M = Sc case, signalizes that the oscillations with large magnitude can be generated weakly changing the energy of the whole crystal. The computed mean square displacements of M atoms $\langle u^2 \rangle$ follows the degree of mode anharmonicity, being equal to 0.0058 (Sc), 0.0020 (Lu), 0.0015 (Y), and 0.0012 (La), all in Å^2 and computed for 1 K, thus they follow the same order as superconducting critical temperature T_c.

TABLE VII. The dependence of T_{1u} and T_{2g} modes frequency (in THz) on M atoms' displacement, showing the increasing anharmonicity while going from harmonic M = La, via slightly anharmonic M = Y and Lu, to strongly anharmonic M = Sc.

U (Å)	ScV$_2$Al$_{20}$		YV$_2$Al$_{20}$		LaV$_2$Al$_{20}$		LuV$_2$Al$_{20}$	
	T_{1u}	T_{2g}	T_{1u}	T_{2g}	T_{1u}	T_{2g}	T_{1u}	T_{2g}
0.04	1.980	1.981	2.782	2.941	2.974	3.195	2.093	2.029
0.07	2.024	2.036	2.798	2.962	2.976	3.199	2.098	2.038
0.14	2.154	2.178	2.842	3.004	2.981	3.212	2.124	2.063

This picture agrees very well with the analysis of atomic potential presented previously by Koza *et al.* for Sc and La [50] and Y [51]. The atomic potentials for that atoms supplemented by Lu are also presented in the right panel of Fig. 13. The atomic potentials of M atoms are shown as a dependence of total energy on the single atom displacement $u_{M(8a)}$ along $(x,0,0)$ direction. The solid lines represent the quartic polynomial [$V(u) = au^2 + bu^4$] fits to the calculated data, although the quadratic (harmonic) form to fit the La atomic potential may as well be used. The largest contribution of quartic order is observed for Sc atoms which is clearly apparent in the nonlinear dependence of the restoring force (Hellmann-Feynman force) on displacement presented in the inset. Making a simple comparison of restoring forces generated on the atoms in the cage, the weak bonding of Sc atoms with the cage can be concluded. From the set of Hellmann-Feynman forces [$F(n)$] the force constants [$\Phi(n, m)$] are calculated by solving the set of equations $F(n) = \Sigma_m \Phi(n,m)u(m)$. The computed on-site force constants [$\Phi(n,n)$] for the M atoms are as follows: 1.35 (Sc), 3.85 (Lu), 4.34 (Y), and 7.38 (La), all in eV/Å^2 units, thus

again they organize themselves into three groups, correlated with the observed superconducting critical temperatures. This correlation is not surprising, since the partial electron-phonon coupling constant $\lambda_i \propto \Phi_i^{-1}$, that illustrates the important role of M atom vibrations for the superconductivity in these materials. The smallest force constant (meaning that the smallest force is needed to move the atom) was found for the "most" superconducting ScV$_2$Al$_{20}$ case, whereas it was the largest for nonsuperconducting LaV$_2$Al$_{20}$. The smallest force needed to disturb the atom's position also means that the response from the M atom to the surrounding cage will be the smallest for Sc, so the atom is weakly coupled to its neighbors.

We can conclude that the low-frequency mode anharmonicity is clearly correlated with the magnitude of the superconductivity in MV$_2$Al$_{20}$ caged materials, with LaV$_2$Al$_{20}$ standing out as the only nonsuperconducting system, and T_c enhanced in the most anharmonic ScV$_2$Al$_{20}$. The latter finding is astonishing since other caged compounds containing La, LaT_2Zn$_{20}$ (T = Ru, Ir), are superconducting. Nevertheless, when the phonon spectrum is compared to the results presented
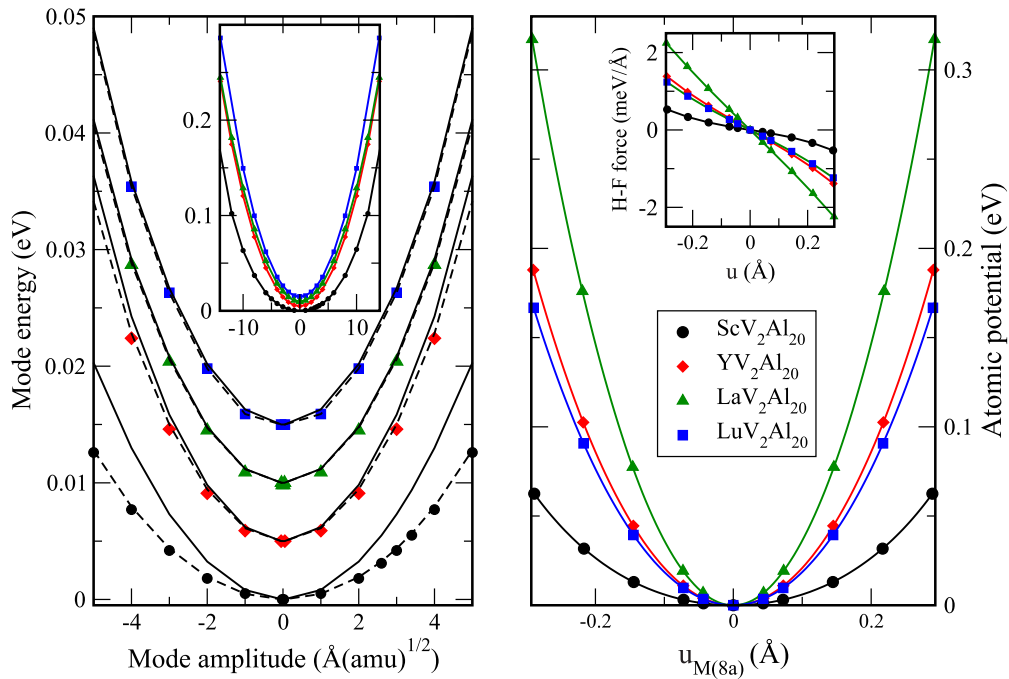

FIG. 13. Left panel: The potential of the T_{2g} mode as a function of mode amplitude in MV$_2$Al$_{20}$ (M = Sc, Y, La, Lu). In the inset the data in a wide amplitudes range are presented. The solid and dashed lines represent, respectively, quadratic and quartic polynomial fits to the data calculated in a wide range. The whole amplitude range is shown in the inset, whereas the difference between the fits are visible in the smaller range, shown in the main panel. Right panel: The atomic potentials calculated for M atoms in MV$_2$Al$_{20}$ (M = Sc, Y, La, Lu). The inset shows the Hellmann-Feynman forces, harmonic only for the La case. Anharmonic character of the T_{2g} mode potential and M atomic potentials in M = Sc, Y, and Lu is visible, especially for the M = Sc case.
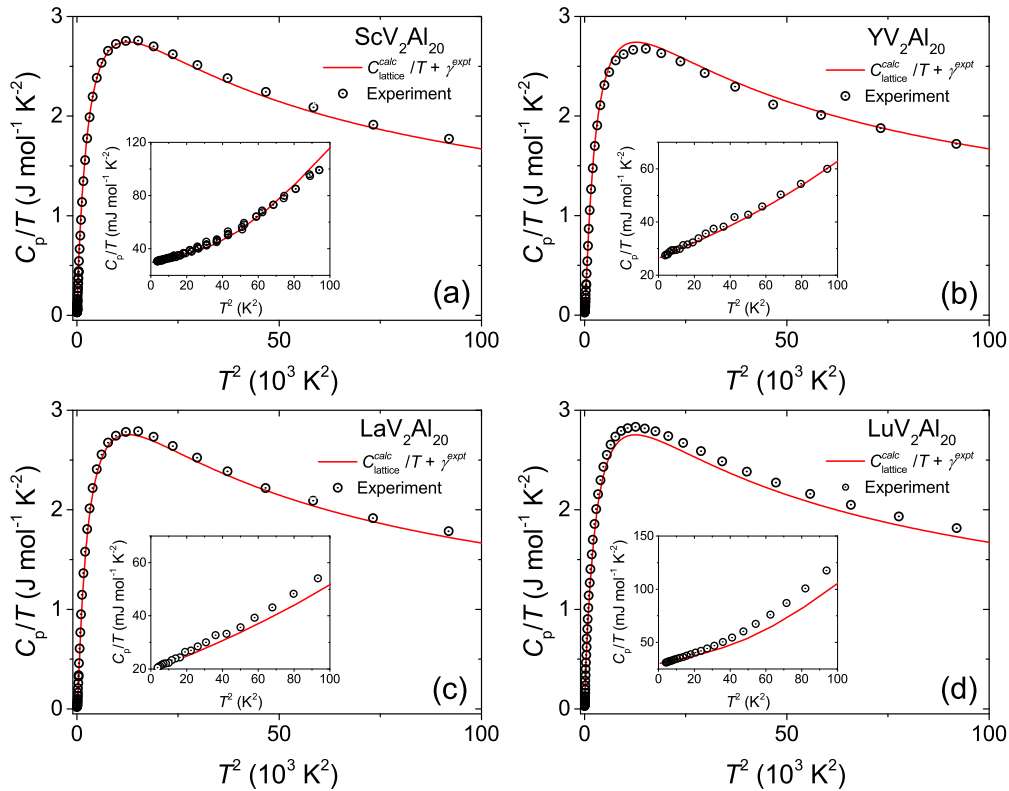
FIG. 14. Comparison of the experimental (dots) and calculated heat capacities. The electronic contribution based on the experimental values of Sommerfeld coefficients (γ) is added to the phonon heat capacity.

for superconducting LaT_2Zn_{20} (T = Ru, Ir) by Hasegawa *et al.* [52] the major difference is seen in the 8a-occupying atom (La) and 16c (Zn) modes. In $LaRu_2Zn_{20}$ the Zn(16c) modes clearly dominate the low-energy part of the phonon DOS separated from the relatively high-energy La(8a) vibrations. This apparent difference with our results can be explained by the differences in crystal structures of MV$_2$Al$_{20}$ and LaT_2Zn$_{20}$. In the latter, La atoms are positioned in smaller cages and the filling factor is even higher than for LaV$_2$Al$_{20}$. Meanwhile the polyhedra centered at Zn(16c) are still much larger than the Zn atom, which explains the presence of low-energy modes. Also, the electronic structure of these two groups of cage compounds will be much different, thus direct comparison between them is not possible, and our conclusion of the role of anharmonicity in the superconductivity of MV$_2$Al$_{20}$ materials cannot be generalized to LaT_2Zn$_{20}$.

To verify the correctness of the phonon spectra, the lattice contribution to the heat capacity was calculated, using the standard formula [86]

$$C_{latt} = C_V = R \int_0^\infty F(\omega) \left(\frac{\hbar\omega}{k_B T}\right)^2 \frac{\exp\left(\frac{\hbar\omega}{k_B T}\right)}{\left(\exp\left(\frac{\hbar\omega}{k_B T}\right)-1\right)^2} d\omega. \quad (6)$$

Assuming that $C_p \approx C_v$, the theoretical results can be compared to the experimental ones, as shown in Fig. 14 (the electronic contribution γT was added to C_{latt}). Agreement between the theory and the measured data is very good, even for the most critical low temperature region. This result shows that the nonlinearity in the C_p/T vs T^2 curve for $T < 10$ K was an inherent feature of the phonon spectra of ScV$_2$Al$_{20}$

and LuV$_2$Al$_{20}$, originating from the large intensity of the low-energy optical phonon modes.

Figure 15 shows the comparison of low-temperature lattice heat capacities of the four compounds. The $\sim T^4$ upturn, correlated with the filling factor of the M-Al cage and

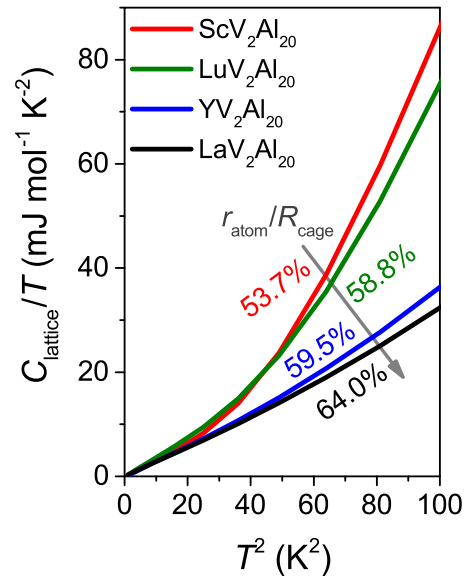
FIG. 15. Comparison of the calculated lattice heat capacities of MV$_2$Al$_{20}$ (M = Sc, Y, La, and Lu). Note the approximately linear character of LaV$_2$Al$_{20}$ and YV$_2$Al$_{20}$ as opposed to clearly visible upturn in case of ScV$_2$Al$_{20}$ and LuV$_2$Al$_{20}$.

TABLE VIII. The average phonon energy (meV) computed using the partial phonon DOS for each of the sublattice and electron-phonon coupling parameters λ_i (atomic population of the sublattices taken into account) of MV$_2$Al$_{20}$ compounds, obtained using the McMillan-Hopfield parameters from Table V. The total λ is a sum over i. The value of T_c is computed using the Allen-Dynes formula and $\mu^* = 0.1$. The values of λ_{ep} parameters calculated within different methods are gathered in Table IX.

M	M	V	Al(96)	Al(48)	Al(16)
Sc			$\sqrt{\langle \omega_i{}^2 \rangle}$		
	8.90	27.57	26.71	30.71	18.28
			λ_i		
	0.221	0.070	0.046	0.026	0.007
	λ_{el-ph} total = 0.37, ω_{log} = 227 K			T_c calc. = 0.60 K	
Y			$\sqrt{\langle \omega_i{}^2 \rangle}$		
	12.44	27.35	26.67	30.6	18.26
			λ_i		
	0.045	0.071	0.046	0.027	0.007
	λ_{el-ph} total = 0.20, ω_{log} = 245 K			T_c calc. = 10^{-4} K	
La			$\sqrt{\langle \omega_i{}^2 \rangle}$		
	13.24	27.63	26.47	30.48	17.20
			λ_i		
	0.014	0.057	0.040	0.022	0.007
	λ_{el-ph} total = 0.14, ω_{log} = 273 K			T_c calc. = 10^{-15} K	
Lu			$\sqrt{\langle \omega_i{}^2 \rangle}$		
	8.30	27.35	26.79	30.64	18.64
			λ_i		
	0.043	0.075	0.046	0.026	0.006
	λ_{el-ph} total = 0.20, ω_{log} = 228 K			T_c calc. = 10^{-4} K	

observed in experimental results for ScV$_2$Al$_{20}$ and LuV$_2$Al$_{20}$, is reproduced in the calculated heat capacity.

Now, using the computed McMillan-Hopfield parameters and the averaged phonon frequencies, the electron-phonon coupling constant λ_{el-ph} and critical temperature T_c can be calculated. The superconducting critical temperature was calculated from the Allen-Dynes formula [87]:

$$T_c = \frac{\omega_{log}}{1.20} \exp\left[\frac{-1.04(1+\lambda)}{\lambda - \mu^*(1 + 0.62\lambda)}\right], \quad (7)$$

with

$$\omega_{log} = \exp\left[\int F(\omega) \ln \omega \frac{d\omega}{\omega} \bigg/ \int F(\omega) \frac{d\omega}{\omega}\right],$$

where F is the total phonon DOS (see Table VIII). Note that the above equation was optimized for $\mu^* = 0.1$ [87] and this value was used in the theoretical computations (ω_{log} values are considerably lower than Debye temperatures). Similarly to the dynamical properties, discussed earlier, the calculated values of λ_{el-ph} are forming three groups, lowest $\lambda_{el-ph} = 0.14$ for the nonsuperconducting $M =$ La case, middle $\lambda_{el-ph} = 0.20$ for $M =$ Y, Lu, and highest $\lambda_{el-ph} = 0.37$ for $M =$ Sc. These values of λ_{el-ph} result in the critical temperatures varying from 0 to 0.60 K. ScV$_2$Al$_{20}$ has the highest calculated $T_c = 0.60$ K versus measured $T_c = 1$ K, and both T_c and λ_{el-ph} are slightly underestimated. Qualitative agreement is observed for the nonsuperconducting LaV$_2$Al$_{20}$, which has the lowest

TABLE IX. Values of the electron-phonon coupling parameter λ_{el-ph} obtained within different approaches: determined from the heat capacity results using relationship shown in Eq. (4) (repeated from Table III), estimated from the comparison of experimental and theoretical values of the Sommerfeld coefficient γ (Table IV), and calculated from the McMillan-Hopfield (MH) parameters and the phonon DOS (Table VII). For comparison, experimental and calculated values of T_c are also repeated after Tables III and VII.

M	Sc	Y	La	Lu
λ_{el-ph}				
Calculated from heat capacity results using Eq. (4)	0.41	0.39		0.39
Calculated from the relationship $\gamma_{expt} = \gamma_{calc}(1 + \lambda_{el-ph})$	0.40	0.43	0.03	0.59
Calculated from MH and the phonon DOS (see Table VII)	0.37	0.20	0.14	0.20
T_c (K)				
Experimental	1.00	0.60		0.57
Calculated	0.60	10^{-4}	10^{-15}	10^{-4}

calculated λ_{el-ph} and zero T_c. More serious underestimation is seen for YV$_2$Al$_{20}$ and LuV$_2$Al$_{20}$, the value of $\lambda_{el-ph} = 0.20$ obtained by the RMTA approach, results in $T_c \approx 0$ K, instead of the measured $T_c \approx 0.6$ K. If the Allen-Dynes formula (7) and the computed values of ω_{log} are used for T_c calculation, λ around 0.35 would be required to give $T_c \sim 0.5$ K, as in the experiment for those two materials. The absolute difference between the expected and calculated values of λ_{el-ph} is not large (0.15), but in the weak-coupling regime any small underestimations of λ_{el-ph} result in large deviations in T_c (see Table IX). There are several possible reasons of the underestimation of λ_{el-ph} connected to the main assumptions of the RMTA approach, used here (see [78,79], and references therein). The first and most likely reason is the rigid ion approximation, in which it is assumed that the atomic potential moves rigidly with the vibrating atom. It works well for the transition metals and much worse for sp-like elements, due to delocalization of these electronic states and poor potential screening. This usually leads to the underestimation of the electron-phonon coupling parameters in such materials. As our compounds are mainly built from p-like Al atoms, underestimation of Al contribution of λ_{el-ph} in RMTA is expected, and may explain too small values of λ_{el-ph} among all of the superconducting MV$_2$Al$_{20}$ compounds. Nevertheless, the relative differences even in the underestimated values of electron-phonon coupling allow us to understand the role of each atoms' group in determining the superconducting state in this series of materials, since it is reasonable to expect that the "background" contribution to λ_{el-ph} among all three superconducting materials will be equally lowered. This is supported by almost the same values of η_{Al} for superconducting $M =$ Sc, Y, and Lu, being only lower for the nonsuperconducting $M =$ La. Especially, the role of M atom and enhancement of T_c in ScV$_2$Al$_{20}$, induced by the rattlinglike Sc vibrations, becomes evident. Considerably lower $\lambda_{Lu/Y}$ values, when compared to λ_{Sc}, result in a smaller total coupling parameter, since Al and V contributions remain similar for the three superconducting materials. This smaller

$\lambda_{\text{Lu/Y}}$ is related to smaller values of the McMillan-Hopfield parameters on Lu/Y and, especially, much larger product of masses and average vibration frequencies ($M_i\langle\omega_i^2\rangle$) of these elements, which is in the denominator in Eq. (5). The effect of the decrease in mass of M, when going from Lu to Y and Sc, is compensated only for the Y case by the increase in the vibrational frequency ($\langle\omega_i^2\rangle$), since the interatomic force constant of Lu and Y are similar, ensuring that $M_{\text{Lu}}\langle\omega_{\text{Lu}}^2\rangle \approx M_{\text{Y}}\langle\omega_{\text{Y}}^2\rangle$. Scandium does not follow this rule, and due to much weaker coupling to the Al cage (much smaller force constant Φ) the product $M_{\text{Sc}}\langle\omega_{\text{Sc}}^2\rangle$ is more than 3 times smaller, than for Lu and Y. This weaker coupling to the Al cage, which is also correlated with its anharmonic and rattlinglike behavior, is then effectively increasing Sc contribution to $\lambda_{\text{el-ph}}$, making the T_c the highest among the studied series. The $M = $ La compound behaves in the opposite direction, as its perfect harmonic behavior, correlated with the strongest La-cage bonding and smallest McMillan-Hopfield parameters, remains in clear correlation with its nonsuperconducting behavior.

The additional reason for why the electron-phonon coupling in ScV$_2$Al$_{20}$ is better captured in the performed calculations, comparing to the other systems analyzed, may be related to second assumption of the RMTA approach. In the so-called *local vibration approximation*, $\lambda_{\text{el-ph}}$ in Eq. (5) is decoupled to a sum of contributions from independent crystal sites i, with any off-diagonal terms in $\lambda_{\text{el-ph}}$ neglected (i.e., contributions to the electron-phonon coupling from different i-j sites are not considered, and in $\lambda_{\text{el-ph}} = \sum_{ij}\lambda_{ij}$ we set $\lambda_{ij} = \lambda_i\delta_{ij}$). In our computations, the $M = $ Sc case seems to be best suited for this assumption, as well as for the "rigid-ion" one, since first it is an early transition metal, with the larger localization of its wave functions, while compared to 4d (Y) or 5d (Lu) elements, and second, Sc atoms are less coupled to the cages, due to the flatlike potential and weaker force constant. Thus, the individual contribution $\lambda_i = \eta_i/M_i\omega_i^2$ captures most of its contribution to the total coupling. When the coupling of the M element to the environment becomes stronger (Φ increases), and the Y-4d (Lu-5d) wave functions become less localized, observed underestimations in $\lambda_{\text{el-ph}}$ may suggest that the electron-phonon coupling becomes a more collective property of the cage + filler and decoupling it into site contributions of the Eq. (5) type (with an individual atomic mass in the denominator) does not work that well. Nevertheless, the performed analysis of the McMillan-Hopfield parameters and the atomic contributions to the electron-phonon coupling confirms the important role of the filler atom in determining the superconductivity of the MV$_2$Al$_{20}$ system, and shows the clear correlation of the low-frequency anharmonic Sc vibrations with the enhanced superconducting critical temperature in this compound, along the isoelectronic MV$_2$Al$_{20}$ series.

V. CONCLUSIONS

The results of empirical and theoretical studies of the MV$_2$Al$_{20}$ ($M = $ Sc, Y, La, and Lu) compounds show that those

with $M = $ Sc, Y, and Lu are weakly coupled, type-II BCS superconductors with the electron-phonon coupling constant $\lambda_{\text{el-ph}} \sim 0.4$. Values of $\lambda_{\text{el-ph}}$ and T_c obtained in different ways in this work are summarized in Table IX. The estimated critical temperatures for ScV$_2$Al$_{20}$, YV$_2$Al$_{20}$, and LuV$_2$Al$_{20}$ (1.03, 0.61, and 0.60 K, respectively) are slightly lower than the values reported previously for Al$_x$V$_2$Al$_{20}$ ($\sim$1.5 K) and Ga$_x$V$_2$Al$_{20}$ ($\sim$1.7 K) [42,44]. Two Zn-based CeCr$_2$Al$_{20}$-type compounds: LaIr$_2$Zn$_{20}$ and LaRu$_2$Zn$_{20}$ show superconductivity with comparable T_c (0.6 and 0.2 K, respectively) [37]. Two other examples of CeCr$_2$Al$_{20}$-type superconductor, PrTi$_2$Al$_{20}$ [45] and PrV$_2$Al$_{20}$ [88], exhibit rather exotic behavior, namely the coexistence of superconductivity with a quadrupolar ordering, and thus are not comparable with the compounds discussed here. Similar situation is found in PrIr$_2$Zn$_{20}$, where superconductivity ($T_c \approx 0.05$ K) was found to coexist with an antiferroquadrupolar order [37,89].

The electronic and phonon structure calculations confirmed the weak-coupling regime of the electron-phonon interaction in these materials, and showed the importance of the rattling-like M atom modes in driving them into superconducting state. In particular, direct correlations between the critical temperature T_c and the dynamical characteristics of the M element (vibrational frequencies, force constants, mean square displacements) were encountered: the purely harmonic La compound was not superconducting, the weakly anharmonic Y and Lu had intermediate $T_c \sim 0.6$ K, and finally the strongly anharmonic (rattlinglike) Sc compound had $T_c \sim$ 1 K, considerably enhanced comparing to other materials in the studied isoelectronic series. The rigid muffin tin calculations of $\lambda_{\text{el-ph}}$ allowed us to confirm this trend, giving the highest $\lambda_{\text{el-ph}}$ in ScV$_2$Al$_{20}$, intermediate for $M = $ Y and Lu, and smallest for $M = $ La. The observed underestimations of λ possibly arises because of limitations of the RMTA approach used in the theoretical computations.

The presented results underline the major influence of the cage-filling atom occupying the 8a position in the cubic unit cell of MV$_2$Al$_{20}$ on the overall electron and phonon properties of these materials. This family of intermetallic compounds enables us to cross the border between rattling and harmonic vibrations of the filling atom in a cage that is favorable for superconductivity, allowing us to test and model quantitatively the effect of rattling on the T_c within a single structure type. This feature makes the MV$_2$Al$_{20}$ family an interesting system to study the effect of rattling on superconductivity.

ACKNOWLEDGMENTS

[1] Z. Hiroi, S. Yonezawa, T. Muramatsu, J.-I. Yamaura, and Y. Muraoka, Specific heat of the β-pyrochlore oxide superconductors CsOs$_2$O$_6$ and RbOs$_2$O$_6$, J. Phys. Soc. Jpn. **74**, 1255 (2005).

[2] J.-I. Yamaura, S. Yonezawa, Y. Muraoka, and Z. Hiroi, Crystal structure of the pyrochlore oxide superconductor KOs$_2$O$_6$, J. Solid State Chem. **179**, 336 (2006).

[3] B. C. Sales, D. Mandrus, B. C. Chakoumakos, V. Keppens, and J. R. Thompson, Filled skutterudite antimonides: Electron crystals and phonon glasses, Phys. Rev. B **56**, 15081 (1997).

[4] B. C. Sales, B. C. Chakoumakos, and D. Mandrus, Thermoelectric properties of thallium-filled skutterudites, Phys. Rev. B **61**, 2475 (2000).

[5] S. Sanada, Y. Akoi, H. Akoi, A. Tsuchiya, D. Kikuchi, H. Sugawara, and H. Sato, Exotic heavy-fermion state in filled skutterudite $SmOs_4Sb_{12}$, J. Phys. Soc. Jpn. **74**, 246 (2005).

[6] E. D. Bauer, N. A. Frederick, P.-C. Ho, V. S. Zapf, and M. B. Maple, Superconductivity and heavy fermion behavior in $PrOs_4Sb_{12}$, Phys. Rev. B **65**, 100506(R) (2002).

[7] Y. Nagao, J. Yamaura, H. Ogusu, Y. Okamoto, and Z. Hiroi, Rattling-induced superconductiviy in the β-pyrochlore oxides AOs_2O_6, J. Phys. Soc. Jpn. **78**, 064702 (2009).

[8] J. Kuneš, T. Jeong, and W. E. Pickett, Correlation effects and structural dynamics in the β-pyrochlore superconductor KOs_2O_6, Phys. Rev. B **70**, 174510 (2004).

[9] H. Mutka, M. M. Koza, M. R. Johnson, Z. Hiroi, J.-I. Yamaura, and Y. Nagao, Generalized density-of-states and anharmonicity of the low-energy phonon bands from coherent inelastic neutron scattering response in the pyrochlore osmates AOs_2O_6 (A = K, Rb, Cs), Phys. Rev. B **78**, 104307 (2008).

[10] Z. Hiroi, S. Yonezawa, Y. Nagao, and J. Yamaura, Extremely strong-coupling superconductivity and anomalous lattice properties in the β-pyrochlore oxide KOs_2O_6, Phys. Rev. B **76**, 014523 (2007).

[11] K. Oshiba and T. Hotta, Strong-coupling theory of rattling-induced superconductivity, J. Phys. Soc. Jpn. **80**, 094712 (2011).

[12] K. Oshiba and T. Hotta, Anomalous isotope effect in rattling-induced superconductor, J. Phys. Soc. Jpn. **81**, 114711 (2012).

[13] K. Hattori and H. Tsunetsugu, A possible isomorphic transition in β-pyrochlore compounds, J. Phys. Soc. Jpn. **78**, 013603 (2008).

[14] K. Hattori and H. Tsunetsugu, Strong coupling superconductivity mediated by three-dimensional anharmonic phonons, Phys. Rev. B **81**, 134503 (2010).

[15] T. Fuse and Y. Ōno, First order bipolaronic transition at finite temperature in the Holstein model, J. Phys. Soc. Jpn. **79**, 093702 (2010).

[16] Z. Hiroi, J. Yamaura, and K. Hattori, Rattling good superconductor: β-Pyrochlore oxides AOs_2O_6, J. Phys. Soc. Jpn. **81**, 011012 (2012)

[17] C. W. Chu and H. H. Hill, Boron isotope effect in superconducting zirconium dodecaboride, Science **159**, 1227 (1968).

[18] Z. Fisk, A. C. Lawsom, B. T. Matthias, and E. Corenzwit, Superconducting isotope effect in ZrB_{12}, Phys. Lett. A **37**, 251 (1971).

[19] J. Teyssier, R. Lortz, A. Petrovic, D. van der Marel, V. Filippov, and N. Shitsevalova, Effect of electron-phonon coupling on the superconducting transition temperature in dodecaboride superconductors: A comparison of LuB_{12} with ZrB_{12}, Phys. Rev. B **78**, 134504 (2008).

[20] R. Lortz, R. Viennois, A. Petrovic, Y. Wang, P. Toulemonde, C. Meingast, M. M. Koza, H. Mutka, A. Bossak, and A. San Miguel, Phonon density of states, anharmonicity, electron-phonon coupling, and possible multigap superconductivity in the clathrate superconductors Ba_8Si_{46} and $Ba_{24}Si_{100}$: Factors behind large difference in T_c, Phys. Rev. B **77**, 224507 (2008).

[21] S. Samson, The crystal structure of the intermetallic compound $Mg_3Cr_2Al_{18}$, Acta Crystallogr. **11**, 851 (1958).

[22] S. Samson, The crystal structure of the intermetallic compound $ZrZn_{22}$, Acta Crystallogr. **14**, 1229 (1961).

[23] G. D. Ilyushin and V. A. Blatov, Structures of the $ZrZn_{22}$ family: Suprapolyhedral nanoclusters, methods of self-assembly and superstructural ordering, Acta Crystallogr. Sect. B **65**, 300 (2009).

[24] Y. R. Mahajan, S. D. Kirchoff, and F. H. Froes, Thermal stability of rapidly solidified Al-Ti-Gd alloy, Scr. Metall. Mater. **20**, 643 (1986).

[25] A. G. Jackson, Y. R. Mahajan, and S. D. Kirchoff, Identification of $Al_{20}Ti_2Gd$ precipitates in an aged RST Al-4Ti-4Gd alloy, Scr. Metall. Mater. **20**, 1247 (1986).

[26] S. Niemann and W. Jeitschko, Ternary aluminides AT_2Al_{20} (A = rare earth elements and uranium; T = Ti, Nb, Ta, Mo, and W) with $CeCr_2Al_{20}$-type structure, J. Solid State Chem. **114**, 337 (1995).

[27] V. M. T. Thiede, W. Jeitschko, S. Niemann, and T. Ebel, $EuTa_2Al_{20}$, $Ca_6W_4Al_{43}$ and other compounds with $CeCr_2Al_{20}$ and $Ho_6Mo_4Al_{43}$ type structures and some magnetic properties of these compounds, J. Alloys Compd. **267**, 23 (1998).

[28] C. H. Wang, J. M. Lawrence, E. D. Bauer, K. Kothapalli, J. S. Gardner, F. Ronning, K. Gofryk, J. D. Thompson, H. Nakotte, and F. Trouw, Unusual signatures of the ferromagnetic transition in the heavy fermion compound UMn_2Al_{20}, Phys. Rev. B **82**, 094406 (2010).

[29] P. Wiśniewski, P. Swatek, A. Gukasov, and D. Kaczorowski, Ferromagnetism in UMn_2Al_{20} studied with polarized neutron diffraction and bulk magnetic measurements, Phys. Rev. B **86**, 054438 (2012).

[30] C. Moussa, M. Pasturel, B. Stepnik, and O. Trougait, Experimental study of phase relations in the U-Ti-Al ternary system, Intermetallics **57**, 1 (2015).

[31] A. Uziel, A. I. Bram, A. Venkert, A. E. Kiv, D. Fuks, and L. Meshi, Abrupt symmetry decrease in the ThT_2Al_{20} alloys ($T = 3d$ transition metal), J. Alloys Compd. **648**, 353 (2015).

[32] A. I. Bram, A. Venkert, and L. Meshi, Characterization of new aluminides found in the ThT_2Al_{20} alloys (where T = Ti, V, Mn), J. Alloys Compd. **641**, 1 (2015).

[33] N. Gross, T. Nasch, and W. Jeitschko, Ternary intermetallics with high zinc content: TT'_2Zn_{20} (T = Zr, Hf, Nb; T' = Mn, Fe, Ru, Co, Rh, Ni) with $CeCr_2Al_{20}$-type structure, J. Solid State Chem. **161**, 288 (2001).

[34] M. Daszkiewicz, P. Swatek, and D. Kaczorowski, Crystal structure of UT_2Zn_{20} (T = Fe, Co, Ru, Rh, and Ir) phases, J. Alloys Compd. **517**, 26 (2012).

[35] A. P. Gonçalves, J. C. Waerenborgh, A. Amaro, M. Godinho, and M. Almeida, UFe_2Zn_{20}: A new uranium intermetallic compound, J. Alloys Compd. **271–273**, 456 (1998).

[36] P. Swatek and D. Kaczorowski, Intermediate valence behavior in the novel cage compound $CeIr_2Zn_{20}$, J. Phys.: Condens. Matter **25**, 055602 (2013).

[37] P. Swatek, M. Daszkiewicz, and D. Kaczorowski, Crystal structure of the new compound UOs_2Zn_{20}, J. Alloys Compd. **586**, 754 (2014).

[38] V. W. Burnett, D. Yazici, B. D. White, N. R. Dilley, A. J. Friedman, B. Brandom, and M. B. Maple, Structure and physical properties of RT_2Cd_{20} (R = rare earth, T = Ni, Pd) compounds

with the CeCr$_2$Al$_{20}$-type structure, J. Solid State Chem. **215**, 114 (2014).

[39] H. Nyman, S. Andersson, B. G. Hyde, and M. O'Keeffe, The pyrochlore structure and its relatives, J. Solid State Chem. **26**, 123 (1978).

[40] See Supplemental Material at http://link.aps.org/supplemental/10.1103/PhysRevB.93.134507 for a depiction of different views of CeCr$_2$Al$_{20}$-type structure.

[41] K. Momma and F. Izumi, VESTA 3 for three-dimensional visualization of crystal, volumetric and morphology data, J. Appl. Crystallogr. **44**, 1272 (2011).

[42] T. Klimczuk, M. Szlawska, D. Kaczorowski, J. R. O'Brien, and D. J. Safarik, Superconductivity in the Einstein solid VAl$_{10.1}$, J. Phys.: Condens. Matter **24**, 365701 (2012).

[43] D. J. Safarik, T. Klimczuk, A. Llobet, D. D. Byler, J. C. Lashley, J. R. O'Brien, and N. R. Dilley, Localized anharmonic rattling of Al atoms in VAl$_{10.1}$, Phys. Rev. B **85**, 014103 (2012).

[44] A. Onosaka, Y. Okamoto, J. Yamaura, and Z. Hiroi, Superconductivity in an Einstein solid A$_x$V$_2$Al$_{20}$ (A = Al and Ga), J. Phys. Soc. Jpn. **81**, 023703 (2012).

[45] A. Sakai, K. Kuga, and S. Nakatsuji, Superconductivity in the ferroquadrupolar state in the quadrupolar Kondo lattice PrTi$_2$Al$_{20}$, J. Phys. Soc. Jpn. **81**, 083702 (2012).

[46] T. Onimaru, K. T. Matsumoto, Y. F. Inoue, K. Umeo, Y. Saiga, Y. Matsushita, R. Tamura, K. Nishimoto, I. Ishii, T. Suzuki, and T. Takabatake, Superconductivity and structural phase transitions in caged compounds RT$_2$Zn$_{20}$ (R = La, Pr, T = Ru, Ir), J. Phys. Soc. Jpn. **79**, 033704 (2010).

[47] T. Onimaru, N. Nagasawa, K. T. Matsumoto, K. Wakiya, K. Umeo, S. Kittaka, T. Sakakibara, Y. Matsushita, and T. Takabatake, Simultaneous superconducting and antiferroquadrupolar transitions in PrRh$_2$Zn$_{20}$, Phys. Rev. B **86**, 184426 (2012).

[48] A. Onosaka, Y. Okamoto, J. Yamaura, T. Hirose, and Z. Hiroi, Large diamagnetism of AV$_2$Al$_{20}$ (A = Y and La), J. Phys. Soc. Jpn. **81**, 123702 (2012).

[49] T. Hirose, Y. Okamoto, J. Yamaura, and Z. Hiroi, Large diamagnetic susceptibility from petit Fermi surfaces in LaV$_2$Al$_{20}$, J. Phys. Soc. Jpn. **84**, 113701 (2015).

[50] M. M. Koza, A. Leithe-Jasper, E. Sischka, W. Schnelle, H. Borrmann, H. Mutka, and Yu. Grin, Effect of the electropositive elements A = Sc, La, and Ce on the microscopic dynamics of AV$_2$Al$_{20}$, Phys. Chem. Chem. Phys. **16**, 27119 (2014).

[51] M. M. Koza, H. Mutka, Y. Okamoto, J. Yamaura, and Z. Hiroi, On the microscopic dynamics of the 'Einstein solids' AlV$_2$Al$_{20}$ and GaV$_2$Al$_{20}$, and of YV$_2$Al$_{20}$: A benchmark system for 'rattling' excitations, Phys. Chem. Chem. Phys. **17**, 24837 (2015).

[52] T. Hasegawa, N. Ogita, and M. Udagawa, First-principles calculations of lattice vibrations on LaT$_2$Zn$_{20}$ (T = Ru and Ir), J. Phys.: Conf. Ser. **391**, 012016 (2012).

[53] K. Wakiya, T. Onimaru, S. Tsutsui, T. Hasegawa, K. T. Matsumoto, N. Nagasawa, A. Q. R. Baron, N. Ogita, M. Udagawa, and T. Takabatake, Low-energy optical phonon modes in the caged compound LaRu$_2$Zn$_{20}$, Phys. Rev. B **93**, 064105 (2016).

[54] H. M. Rietveld, A profile refinement method for nuclear and magnetic structures, J. Appl. Crystallogr. **2**, 65 (1969).

[55] J. Rodríguez-Carvajal, Recent advances in magnetic structure determination by neutron powder diffraction, Physica B **192**, 55 (1993).

[56] Quantum Design PPMS Heat Capacity Option User's Manual, 1085-150, Rev. M6 (2015).

[57] G. Brauer, Konstitution der aluminium-vanadin-verbindung VAl$_3$, Z. Elektrochem. Angew. Phys. Chem. **49**, 208 (1943).

[58] S. Grazulis, D. Chateigner, R. T. Downs, A. F. T. Yokochi, M. Quiros, L. Lutterotti, E. Manakova, J. Butkus, P. Moeck, and A. Le Bail, Crystallography Open Database - An open-access collection of crystal structures, J. Appl. Crystallogr. **42**, 726 (2009).

[59] H. Okamoto, Al-V (aluminum-vanadium), J. Phase Equilib. **22**, 86 (2001).

[60] H. Okamoto, Al-Y (Aluminum-yttrium), J. Phase Equilib. Diff. **29**, 114 (2008).

[61] W. H. Baur, The geometry of polyhedral distortions. Predictive relationships for the phosphate group, Acta Crystallogr. Sect. B **30**, 1195 (1974).

[62] See Supplemental Material at http://link.aps.org/supplemental/10.1103/PhysRevB.93.134507 for a plot of relative cage sizes and distortion indices vs covalent radius of the 8a atom.

[63] B. Cordero, V. Gómez, A. E. Platero-Prats, M. Revés, J. Echeverría, E. Cremades, F. Barragána, and S. Alvarez, Covalent radii revisited, Dalton Trans. **21**, 2832 (2008).

[64] R. Higashinaka, A. Nakama, M. Ando, M. Watanabe, Y. Aoki, and H. Sato, Magnetic and transport properties of YbT$_2$Al$_{20}$ (T = Ti, V and Cr), J. Phys.: Conf. Ser. **273**, 012033 (2011).

[65] M. J. Kangas, D. C. Schmitt, A. Sakai, S. Nakatsuji, and J. Y. Chan, Structure and physical properties of single crystal PrCr$_2$Al$_{20}$ and CeM$_2$Al$_{20}$ (M = V, Cr): A comparison of compounds adopting the CeCr$_2$Al$_{20}$ structure type, J. Solid State Chem. **196**, 274 (2012).

[66] See Supplemental Material at http://link.aps.org/supplemental/10.1103/PhysRevB.93.134507 for a full version of the plot of cell parameter vs covalent radius of the 8a atom.

[67] J. Winterlik, G. H. Fecher, A. Thomas, and C. Felser, Superconductivity in palladium-based Heusler compounds, Phys. Rev. B **79**, 064508 (2009).

[68] T. Klimczuk, C. H. Wang, K. Gofryk, F. Ronning, J. Winterlik, G. H. Fecher, J.-C. Griveau, E. Colineau, C. Felser, J. D. Thompson, D. J. Safarik, and R. J. Cava, Superconductivity in the Heusler family of intermetallics, Phys. Rev. B **85**, 174505 (2012).

[69] N. R. Werthamer, E. Helfand, and P. C. Hohenberg, Temperature and purity dependence of the superconducting critical field, Hc2. III. Electron spin and spin-orbit effects, Phys. Rev. **147**, 295 (1966).

[70] A. Tari, in *The Specific Heat of Matter at Low Temperatures* (Imperial College Press, London, 2003), p. 34.

[71] See Supplemental Material at http://link.aps.org/supplemental/10.1103/PhysRevB.93.134507 for a plot of low temperature specific heat for all four compounds.

[72] W. L. McMillan, Transition temperature of strong-coupled superconductors, Phys. Rev. **167**, 331 (1968).

[73] P. Blaha, K. Schwarz, G. K. H. Madsen, D. Kvasnicka, and J. Luitz, *WIEN2K, An Augmented Plane Wave + Local Orbitals Program for Calculating Crystal Properties* (Karlheinz Schwarz, Technische Universität Wien, 2001).

[74] J. P. Perdew, K. Burke, and M. Ernzerhof, Generalized Gradient Approximation Made Simple, Phys. Rev. Lett. **77**, 3865 (1996).

[75] A. Bansil, S. Kaprzyk, P. E. Mijnarends, and J. Toboła, Electronic structure and magnetism of $Fe_{3-x}V_xX$ (X = Si, Ga, and Al) alloys by the KKR-CPA method, Phys. Rev. B **60**, 13396 (1999).

[76] J. J. Hopfield, Angular momentum and transition-metal superconductivity, Phys Rev. **186**, 443 (1969).

[77] G. D. Gaspari and B. L. Gyorffy, Electron-Phonon Interactions, d Resonances, and Superconductivity in Transition Metals, Phys. Rev. Lett. **28**, 801 (1972).

[78] I. I. Mazin, S. N. Rashkeev, and S. Y. Savrasov, Nonspherical rigid-muffin-tin calculations of electron-phonon coupling in high-T_c perovskites, Phys. Rev. B **42**, 366 (1990).

[79] B. Wiendlocha, J. Tobola, and S. Kaprzyk, Search for Sc_3XB (X = In, Tl, Ga, Al) perovskites superconductors and proximity of weak ferromagnetism, Phys. Rev. B **73**, 134522 (2006).

[80] V. K. Ratti, R. Evans, and B. L. Gyorffy, The volume dependence of the electron-phonon mass enhancement and the pressure dependence of T_c in transition metals, J. Phys. F: Met. Phys. **4**, 371 (1974).

[81] B. Wiendlocha, M. J. Winiarski, M. Muras, C. Zvoriste-Walters, J.-C. Griveau, S. Heathman, M. Gazda, and T. Klimczuk, Pressure effects on the superconductivity of the $HfPd_2Al$ Heusler compound: Experimental and theoretical study, Phys. Rev. B **91**, 024509 (2015).

[82] G. Kresse and J. Furthmüller, Efficiency of *ab-initio* total energy calculations for metals and semiconductors using a plane-wave basis set, Comput. Mater. Sci. **6**, 15 (1996).

[83] G. Kresse and J. Furthmüller, Efficient iterative schemes for *ab initio* total-energy calculations using a plane-wave basis set, Phys. Rev. B **54**, 11169 (1996).

[84] K. Parlinski, Z.-Q. Li, and Y. Kawazoe, First-Principles Determination of the Soft Mode in Cubic ZrO_2, Phys. Rev. Lett. **78**, 4063 (1997).

[85] K. Parlinski, Computer code PHONON, Cracow, 2008.

[86] G. Grimvall, *Thermophysical Properties of Materials* (Elsevier, Amsterdam, 1999).

[87] P. B. Allen and R. C. Dynes, Transition temperature of strong-coupled superconductors reanalyzed, Phys. Rev. B. **12**, 905 (1975).

[88] M. Tsujimoto, Y. Matsumoto, T. Tomita, A. Sakai, and S. Nakatsuji, Heavy-Fermion Superconductivity in the Quadrupole Ordered State of PrV_2Al_{20}, Phys. Rev. Lett. **113**, 267001 (2014).

[89] T. Onimaru, K. T. Matsumoto, Y. F. Inoue, K. Umeo, T. Sakakibara, Y. Karaki, M. Kubota, and T. Takabatake, Antiferro-quadrupolar Ordering in a Pr-Based Superconductor $PrIr_2Zn_{20}$, Phys. Rev. Lett. **106**, 177001 (2011).